

Cathode Materials for Rechargeable Magnesium and Lithium Batteries
(マグネシウム及びリチウム二次電池正極材料の開発)

Yunpeng Gu
(谷 雲鵬)

Contents

1	Background	3
1.1	Batteries for the electrical energy storage	3
1.2	Insertion-type electrode materials used in rechargeable batteries	4
1.3	Electrode performance is affected by the electronic structure.....	6
1.3.1	The cell voltage and Fermi levels of electrodes	6
1.3.2	Voltage curves and the density of states on insertion.....	8
1.3.3	Structural distortions and the Jahn-Teller effect	8
1.3.4	Research of electrode materials by <i>ab initio</i> calculation	10
2	Experimental	13
2.1	Sample preparation and characterization	13
2.2	Electrochemical measurements	13
3	Cathode materials for rechargeable lithium batteries	15
3.1	Electrode performance deteriorations caused by the lattice strain	15
3.2	How to design "zero-strain" materials - Suppression of the lattice distortion by itinerant t_{2g} orbitals	16
3.3	A new "zero-strain" cathode material: LiRh_2O_4	17
3.3.1	Sample preparation.....	18
3.3.2	Cathode performance of LiRh_2O_4	19
3.3.3	Evidence of the two-phase Li insertion in $\text{Li}_{1+x}\text{Rh}_2\text{O}_4$	20
3.3.4	A small lattice distortion in $\text{Li}_{1+x}\text{Rh}_2\text{O}_4$ - The "zero-strain" behavior.....	22
4	Cathode materials for rechargeable magnesium batteries	25
4.1	Motivation - Magnesium batteries as an alternative to lithium	25
4.2	Difficulties in making rechargeable magnesium batteries	25
4.2.1	Magnesium metal is inactive in most conventional electrolytes	26
4.2.2	Cathode irreversibility by strong Coulomb interactions from Mg ions	30
4.2.3	Most approaches so far only achieved poor cathode performance	30
4.3	Strategies in this study - Design materials focusing on the electronic picture ..	31
4.3.1	Cluster structures moderate the drastic valence change on Mg insertion..	32
4.3.2	Use hybridized $d-p$ orbitals to create "electronic cluster" structures	33
4.3.3	Candidate materials proposed with strong $d-p$ orbital hybridization	35

4.4	Magnesium battery cathode material: TiSe_2	37
4.4.1	Reversible charge-discharge reactions in Mg/TiSe_2	39
4.4.2	Reversible changes of structural parameters in Mg_xTiSe_2	40
4.4.3	Enhanced electrode performance in TiSe_2 by itinerant $4p$ orbitals - Comparison between Mg_xTiS_2 and Mg_xTiSe_2	45
4.5	Magnesium battery cathode material: TiS_3	48
4.5.1	Material synthesis.....	50
4.5.2	Reversible charge-discharge reactions in Mg/TiS_3	51
4.5.3	The possibility of high storage capacity - Rate capability of Mg_xTiS_3	52
4.6	Roles of d - p hybridization in magnesium battery electrodes	54
4.6.1	Larger capacities are observed in d - p hybridized systems.....	54
4.6.2	Itinerant $4p$ orbitals effectively hybridize with d orbitals and display superior electrode performance to $3p$ systems.....	56
4.6.3	Further discussions on the effect of M-X coordination in MX_2	58
4.7	Perspectives for future research on magnesium batteries	61
5	Supplementary Information.....	62
5.1	The equilibrium potential in a two-phase reaction	62
5.2	Additional results of materials as magnesium battery cathodes.....	63
6	References	64
7	List of Publications	70
8	List of Patents.....	70
9	List of Presentations	70
	Acknowledgement.....	71

Chapter 1: Background

1 Background

1.1 Batteries for the electrical energy storage

Batteries have been being developed to power the increasing worldwide applications for electrical energy storage since the nineteenth century (Figure 1.1). Emissions of carbon dioxide from combustion reactions have driven the global climate change, whereas battery devices can store energy especially from renewable sources such as the wind and solar power, and provide a steady energy supply and efficient energy use to address today's power shortage.

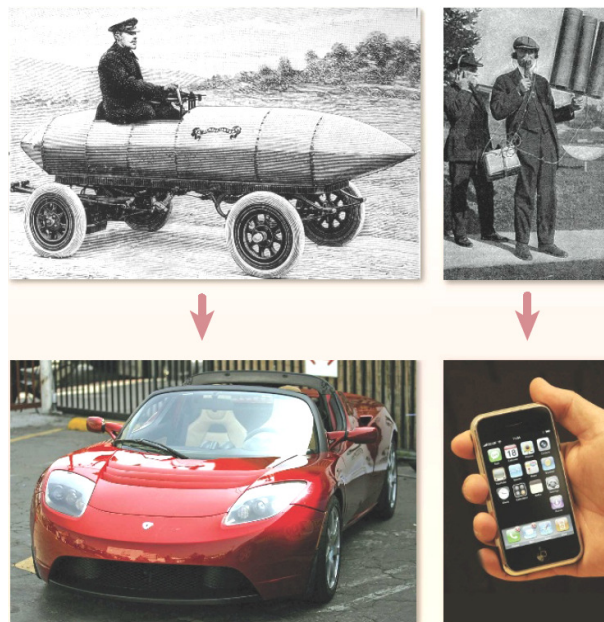


Figure 1.1 Electric vehicles: (top left) *La Jamais Contente*, an electric vehicle equipped with lead-acid batteries in 1899 (also the first vehicle to go over 100 km/h); (bottom left) Tesla roadster, today's electric vehicle with lithium-ion batteries. Communication devices: (top right) The first wireless communication device in Pennsylvania in 1920; (bottom right) The latest mobile phone.[1]

A battery is composed of two electrodes connected by an ionically conductive electrolyte. When these electrodes are connected with an external device, electrons spontaneously flow from the electrode with a more negative potential (anode) to the one with a more positive potential (cathode). An electrolyte is both an electronic insulator

and ionic conductor, which is placed between the two electrodes to force electrons to flow through an external circuit while allowing working ions to flow inside the battery during electrochemical reactions. In rechargeable batteries, a larger voltage applied in the opposite direction can cause the battery to recharge.

1.2 Insertion-type electrode materials used in rechargeable batteries

Rechargeable batteries can date from lead-acid and nickel-cadmium (Ni-Cd) batteries in the nineteenth century, followed by more recent nickel-metal hydride (Ni-MH) and lithium-ion batteries. Ni-MH batteries are used to power hybrid vehicles and cheaper electronics, while lithium-ion batteries with a higher energy density are now being used in high-end electronics and electric vehicles. In a lithium-ion battery the same lithium ion is reversibly inserted into and extracted from the electrode materials, and accompanied by addition and removal of electrons (Figure 1.2).

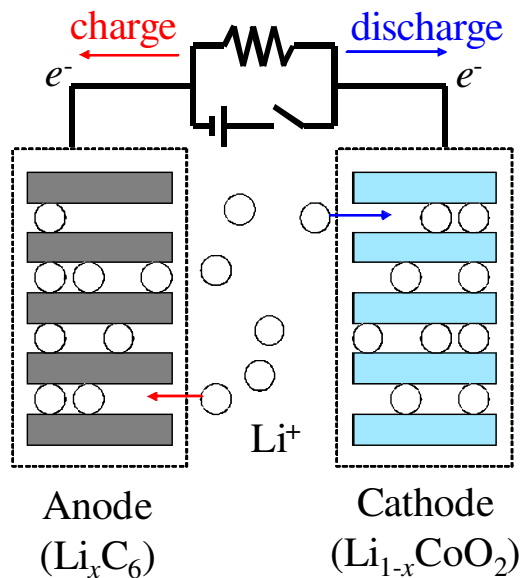


Figure 1.2 An example of the lithium-ion battery. Lithium ions (Li^+) are reversibly inserted into or extracted from the electrode, accompanied by the electron flow (e^-), during charge and discharge reactions.

Insertion electrode materials are widely used in rechargeable batteries because the electrochemical insertion reaction is principally simple and could be highly reversible. Until now material research has been focused on the structural features of host materials to look for available void spaces for guest ions. For example, numerous electrode

materials proposed for lithium-ion batteries can be basically categorized by structural dimension (Figure 1.3): one-dimensional, two-dimensional and three-dimensional compounds.[2]

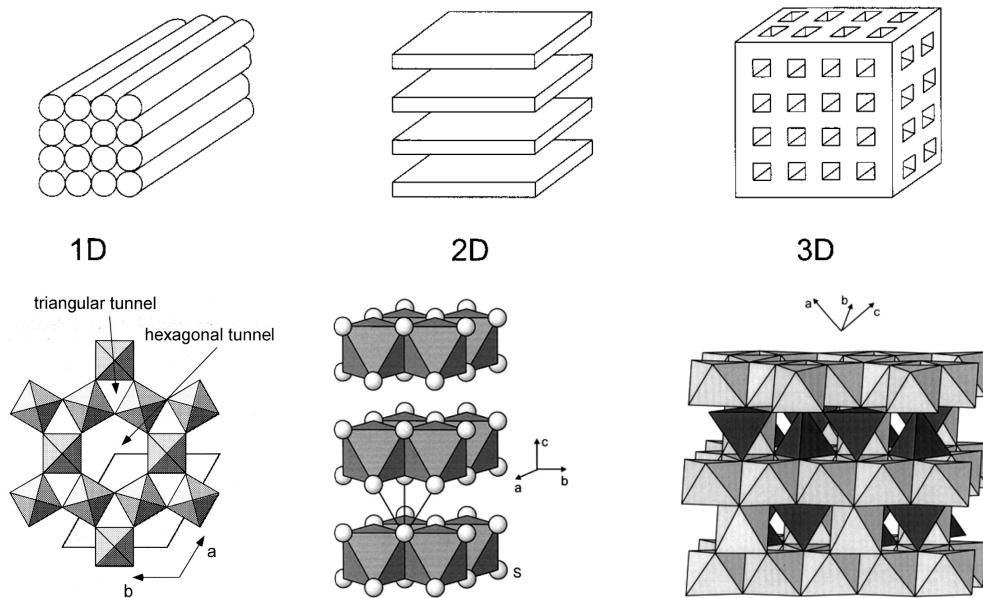


Figure 1.3 Structural classification and examples of electrode materials by the type of void spaces.[2] 1D (left): $h\text{-WO}_3$, with a one-dimensional tunnel structure;[3] 2D (middle): TiS_2 , with a two-dimensional layered structure; 3D (right): LiMn_2O_4 , with a three-dimensional spinel structure.

Generally there are two types of electrode reactions, which have been classified as solid solution reactions and two-phase reactions. A solid solution reaction involves changes in the composition of a single-phase electrode, by insertion or extraction of guest ions into or out of its crystal structure. On the other hand, a two-phase reaction involves changes in the relative amounts of two phases coexisting in the electrode structure, but not the compositions of each phase.

The important differences between these two types of reactions are the different shapes of their discharge curves. The electrode potential in solid solution reactions varies with the concentration of inserted ions, resulting in sloped voltage-capacity curves during discharge or recharge (Figure 1.4 (a)). The electrode potential in two-phase reactions is independent of the electrode composition since there are no available degrees of freedom, so that it will exhibit a constant voltage plateau (Figure 1.4 (b)). The thermodynamics of two-phase reactions is explained further in Section 5.1.

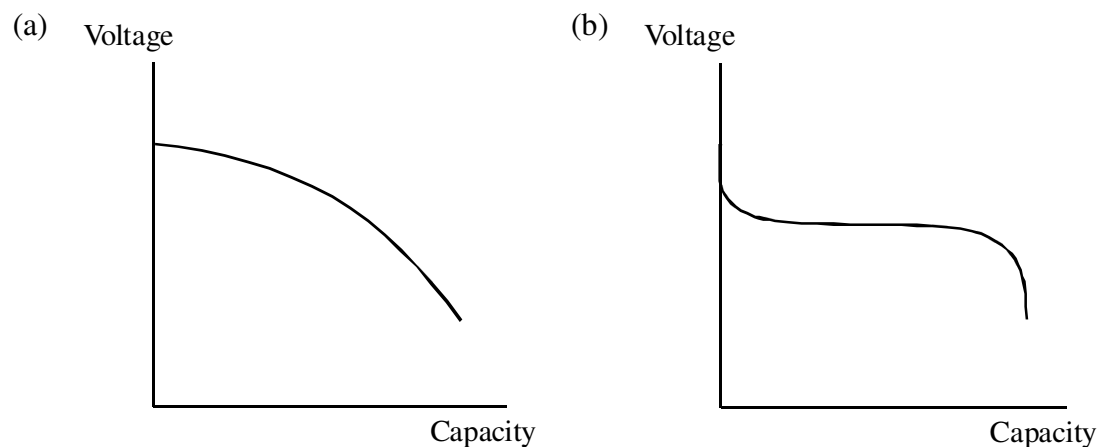


Figure 1.4 Schematic discharge curves of the two types of insertion electrodes: (a) a sloped voltage curve in solid solution (or single-phase) reactions; (b) a flat voltage curve in two-phase reactions.

1.3 Electrode performance is affected by the electronic structure

Electron transfer is always involved during the insertion process of guest ions, thus we suggest in this study that in order to develop new electrode materials, such an electronic process should be equally and worthy investigated as well as the crystal structure. By changing the viewpoint from electrochemistry to solid state physics, one will find that electrode performance is also determined by the electronic structure.

1.3.1 The cell voltage and Fermi levels of electrodes

The cell voltage could be viewed as the difference of Fermi levels (E_F) between anode and cathode materials (Figure 1.5 (a)). In other words, the cell's EMF (electromotive force) would be described as a variation of the electrostatic potential (ϕ). If a metal anode is used, then the operating potential is almost determined by the Fermi level of the cathode, because the Fermi level of the anode remains constant during electrode reactions. While in electrochemistry, the voltage would be viewed as proportional to a variation of the electron electrochemical potential (μ_e), or the difference of chemical potentials of lithium (μ_{Li}) in cathode and anode materials, which are locally determined by electrode reactions at each side.

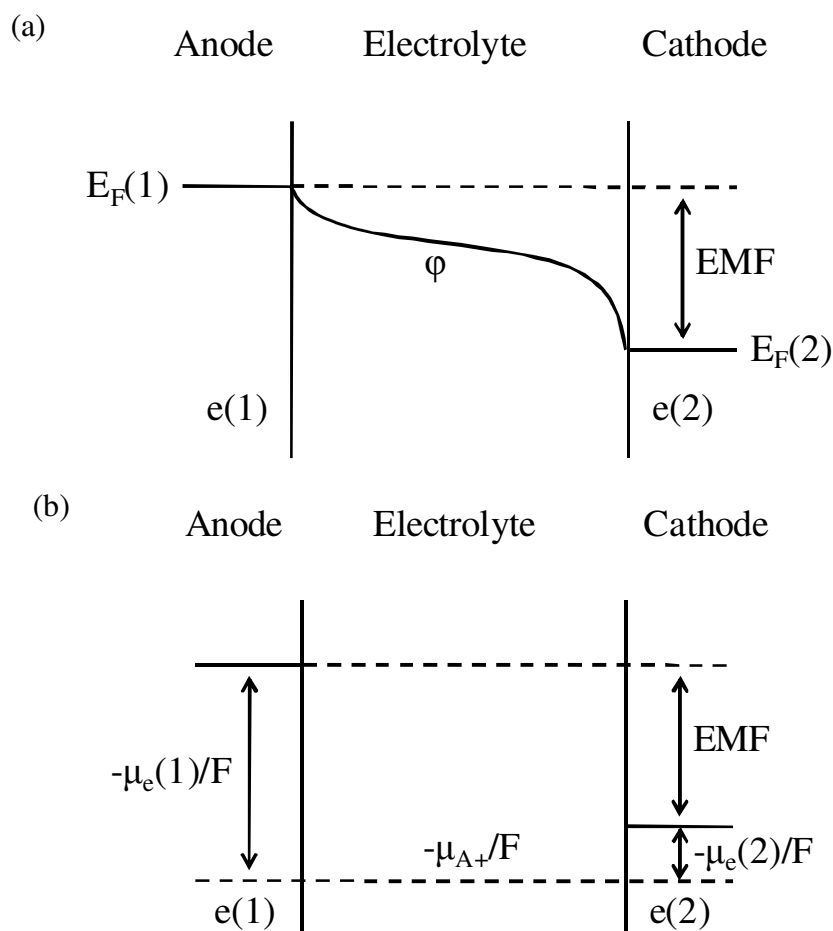


Figure 1.5 Determination of the cell voltage from different points of view: (a) in solid state physics; (b) in electrochemistry.

The cell voltage is thermodynamically stable between energies of the LUMO (lowest unoccupied molecular orbital) and the HOMO (highest occupied molecular orbital) of the electrolyte (Figure 1.6). The energy gap (E_g) between the LUMO and the HOMO is referred to as the electrochemical window of the electrolyte. It is essential to match the electrode Fermi levels (or the EMF) to the electrochemical window. Otherwise the presence of passivation layers is needed to block side reactions for an $EMF > E_g$ case, at one or both solid/electrolyte interfaces (SEI) of electrodes. For example, SEI layers are usually formed at the surface of lithium battery anodes, due to the higher Fermi level (or the more negative chemical potential) of lithium in the anode, compared to the LUMO level of common electrolyte ($E_F(1) > LUMO$).

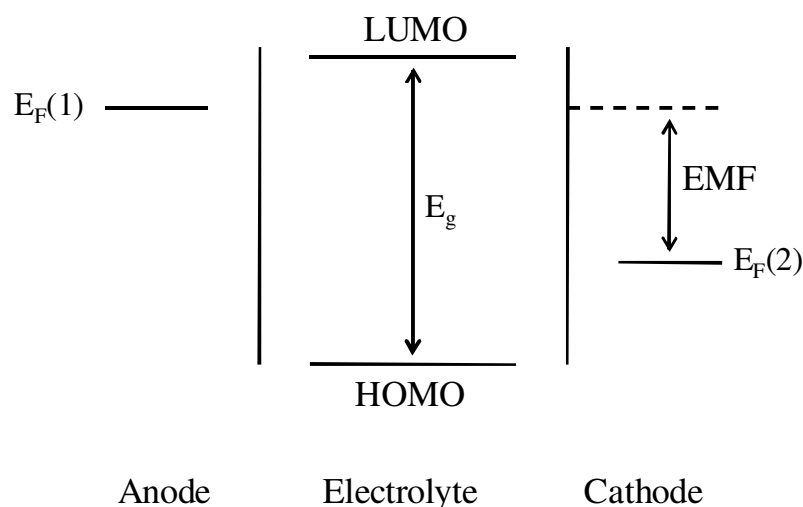


Figure 1.6 The electrochemical window of the electrolyte with its HOMO and LUMO energies relative to the electrode Fermi levels.

1.3.2 Voltage curves and the density of states on insertion

The shape of voltage curves during insertion reactions would be determined by the density of states near the electrode Fermi level, and varies with the concentration of inserted electrons (or guest ions). Given the same amount of available sites for electrons, a higher density of states would result in a gradual voltage curve (Figure 1.7 (a)), since more electrons would insert into the electrode at a particular site energy. On the other hand, a lower density of states produces a steep voltage curve on insertion (Figure 1.7 (b)). Because the cell voltage is usually determined by the Fermi level of the cathode as discussed in Section 1.3.1, materials with a higher density of states would have more storage capacity especially when the voltage range is limited by the electrochemical window of the electrolyte.

1.3.3 Structural distortions and the Jahn-Teller effect

It is commonly known that structural distortions of electrode materials lead to a cycle life deterioration. One of the major causes for the structural distortion is the Jahn-Teller effect, which is often observed when a set of degenerate orbitals of transition metal ions are partially occupied by electrons during the charge-discharge process (Figure 1.8). In practical electrode materials, the Jahn-Teller effect should be suppressed as much as possible to improve their cycle performance.

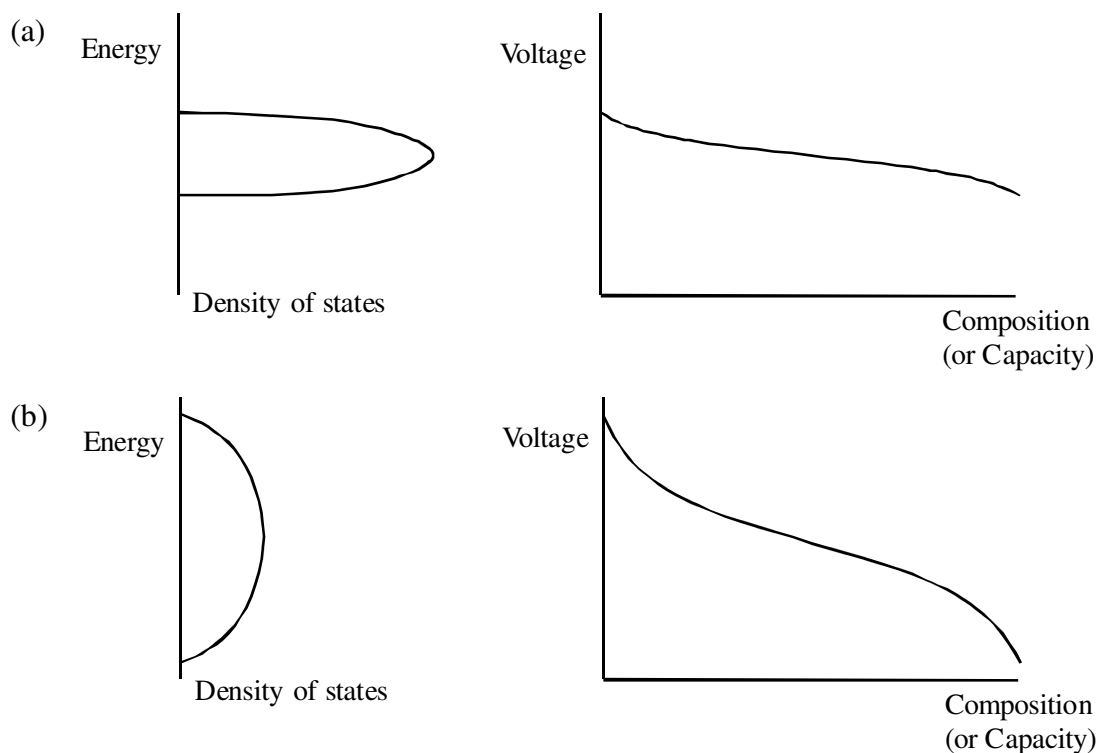


Figure 1.7 The density of states for site energies and shapes of discharge curves on the insertion of guest ions: (a) narrowly distributed site energies with a high density of states and a gradual voltage-composition curve; (b) widely distributed site energies with a low density of states and a steep voltage-composition curve.

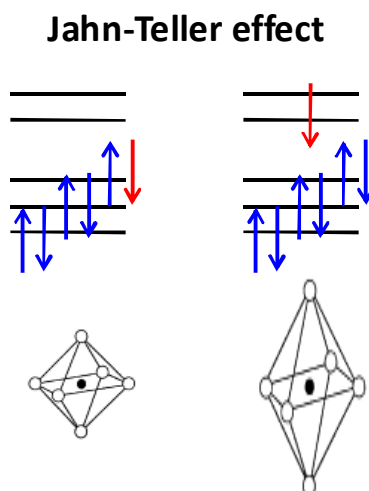


Figure 1.8 Schematic illustrations of the Jahn-Teller effect when an electron entering low-spin d^5 (left) and d^6 (right) systems. A Jahn-Teller effect occurs when the single electron occupies upper e_g orbitals (right), while the Jahn-Teller effect is completely suppressed in filled lower t_{2g} orbitals (left).

1.3.4 Research of electrode materials by *ab initio* calculation

A new way to study electrode materials is by performing *ab initio* calculations (or the first principles techniques). It is possible to investigate how electronic phases or structural changes of electrodes are affected by inserted guest ions. Thermodynamic and kinetic stability of electrodes at different states of charge could also be predicted. Examples of the *ab initio* calculation are given in the following text.

Changes in the electronic structure of electrodes during charge-discharge reactions could be obtained from the calculated density of states. For example, in Li_xCoO_2 , a cathode material of lithium-ion batteries, the density of states in its discharged phase ($x = 1$) shows low-spin Co^{3+} (d^6) without any spin polarization (Figure 1.9 (a) and (c)). While in the charged phase ($x = 0$), down-spin t_{2g} orbitals shifting to a higher energy contributes to the change in the density of states (Figure 1.9 (b) and (d)), which indicates a decrease of valance electrons in the t_{2g} orbitals (d^6 to d^5 , or Co^{3+} to Co^{4+}).

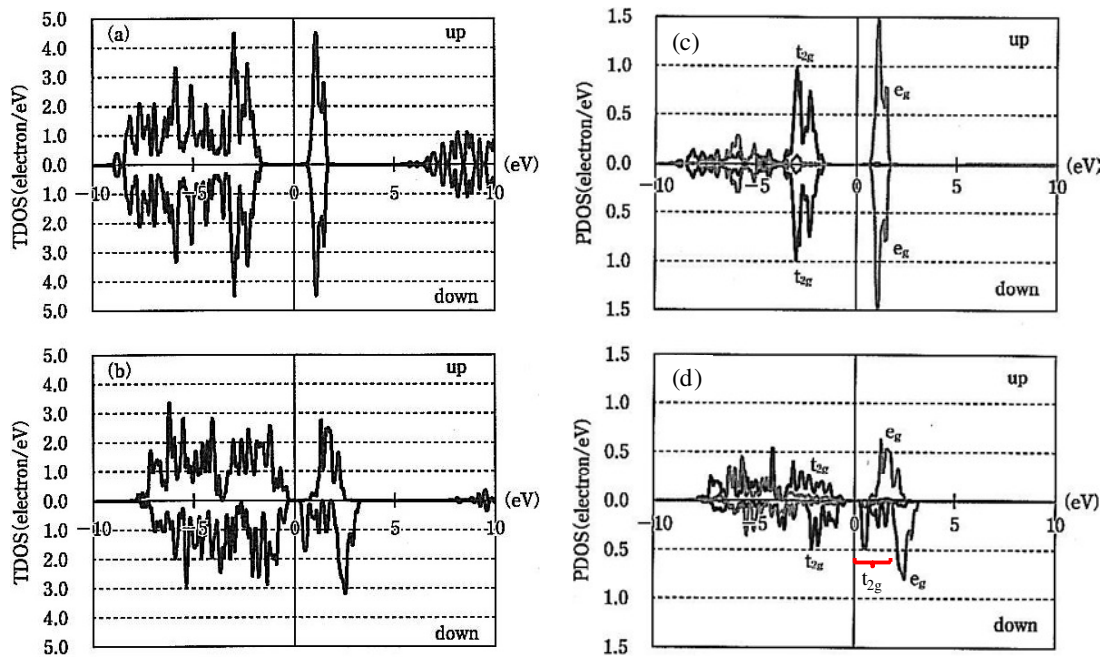


Figure 1.9 The calculated density of states in Li_xCoO_2 using the PAW method with LSDA + U ($U = 5.0$ eV): (a) Total density of states at $x = 1$; (b) Total density of states at $x = 0$; (c) Projected density of states for d orbitals of Co at $x = 1$; (d) Partial density of states for d orbitals of Co at $x = 0$, where the shift of t_{2g} is marked in red.[4]

The cell voltage can be estimated from *ab initio* calculations. Firstly, the very small entropy change (ΔS) is neglected at ambient temperature for electrochemical reactions, which links the average voltage (\bar{V}) to the change in enthalpy (ΔH):

$$\bar{V} = -\frac{\Delta G}{(x_2 - x_1)F} = -\frac{\Delta H - T\Delta S}{(x_2 - x_1)F} \cong -\frac{\Delta H}{(x_2 - x_1)F}$$

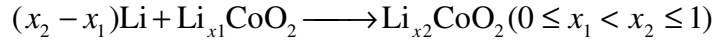
ΔH is further simplified due to the negligible $\Delta(pV)$ in the solid state of electrode materials:

$$\Delta H = \Delta U - \Delta(pV) \cong \Delta U \equiv \Delta E_{total}$$

Thus the average voltage is calculated from total energies (or called the internal energy in thermodynamics) of each product and reactant in an electrochemical reaction:

$$\bar{V} = -\frac{\Delta E_{total}}{(x_2 - x_1)F} = -\frac{1}{(x_2 - x_1)F} \{ \sum E_{total}(\text{product}) - \sum E_{total}(\text{reactant}) \}$$

For example, the following electrochemical reaction is calculated to be $\bar{V} = 4.28$ V using the same method described in Figure 1.9 [4]. The calculated value is in accordance with experimental results (4.2 V vs Li/Li⁺ at $x = 0.5$).



The migration of transition metal ions in electrodes, which severely affects the electrode performance during electrochemical cycling, has also been discussed by calculating the formation energy of different electrode structures.[5] In the layered cathode materials of lithium-ion batteries, such a migration process would cause its structure to transform into a spinel-like structure. The structural transformation involves an intermediate phase in which transition metal ions occupy partial tetrahedral sites (the partially inverse spinel structure in Figure 1.10). In layered Li_xMnO_2 , the Mn migration is favorable because it has a negative energy barrier at $x = 0.5$ (Figure 1.10 top). Although spinel LiCo_2O_4 is thermodynamically stable at $x = 0.5$, a positive energy barrier makes the tetrahedral Co unfavorable in the layered $\text{Li}_{1/2}\text{CoO}_2$ (Figure 1.10 bottom).

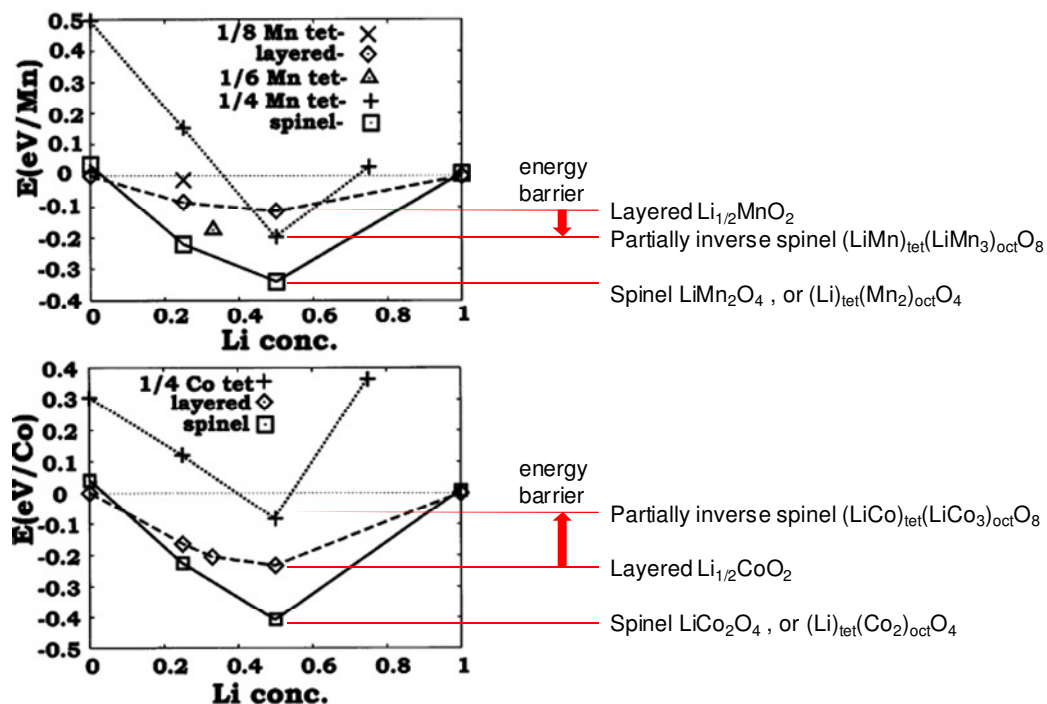


Figure 1.10 Variation of calculated formation energy with Li concentration for three structures of Mn oxides (top) and Co oxides (bottom) using the VASP method: (◇) layered Li_xMO_2 ; (+) Partially inverse spinel $(\text{Li}_x\text{M})_{\text{tet}}(\text{Li}_y\text{M}_3)_{\text{oct}}\text{O}_8$; (□) Spinel $\text{Li}_x\text{M}_2\text{O}_4$. Guidelines of energy barriers are drawn to show the kinetic stability of the layered compounds. [5]

In this study, band structure and density of states calculations were performed to investigate possible orbital hybridizations in electrodes and the presence of band gaps near the Fermi level, which will be discussed in Section 4.4, 4.5 and 4.6.3.

Chapter 2: Experimental

2 Experimental

2.1 Sample preparation and characterization

All samples were synthesized by solid state reaction. Details are described in the section of each material. Structural characterization of synthesized samples was performed by powder X-ray diffraction using a SmartLab X-ray diffractometer (Rigaku Co.), with a graphite monochromatized CuK α radiation source ($\lambda = 1.54184 \text{ \AA}$). Particle sizes of the samples were observed by Scanning Electron Microscopy (SEM). Band structure and density of states (DOS) calculations were performed by the program WIEN2K using the PBE-GGA method.

In the *ex situ* structural analysis of electrodes, electrochemically prepared electrode samples were sealed with polyethylene-nylon films in an argon-filled glovebox before X-ray diffraction measurements, or were measured immediately after being transferred out of the glovebox for preliminary results. Electrode samples for synchrotron X-ray diffraction were sealed in capillary tubes. The synchrotron X-ray diffraction was performed at Photon Factory of High Energy Acceleration Research Organization (KEK-PF), and Rietveld analysis was applied using the program TOPAS Academic. Details are described in Section 4.4.2.

Chemical analysis of electrode samples was performed at Toray Research Center using Inductively Coupled Plasma - Atomic Emission Spectroscopy (ICP-AES).

2.2 Electrochemical measurements

2032-type coin cells for electrochemical measurements were assembled in an argon-filled glovebox. Electrodes were fabricated using the synthesized material, acethylene black and polytetrafluoroethylene in a mass ratio of 81:9:10. The lithium battery cell consists of a cathode, a lithium metal anode and the LiPF₆ electrolyte dissolved at 1 M in ethylene carbonate-dimethyl carbonate 1:1 (v/v). The magnesium battery cell consists of a cathode, a magnesium metal anode and the Mg(AlCl₂EtBu)₂ electrolyte dissolved at 0.25 M in tetrahydrofuran. Electrochemical measurements were conducted using a galvanostatic instrument (Model 1470E Multichannel Potentiostat /

CellTest System, from Solartron Analytical; Model 580 Battery Test System, from Scribner Associates Inc.) by applying a constant current to the cells.

Three-electrode magnesium battery cells were constructed with a cathode as the working electrode, a magnesium metal anode as the counter electrode, a Ag/AgNO₃ (0.25 M) electrode in acetonitrile as the reference electrode and the Mg(ClO₄)₂ electrolyte dissolved at 1 M in acetonitrile. A constant current was applied between working and counter electrodes. The voltage difference between working and reference electrodes was measured during the electrochemical test.

Chapter 3: Cathode materials for rechargeable lithium batteries

3 Cathode materials for rechargeable lithium batteries

3.1 Electrode performance deteriorations caused by the lattice strain

Rechargeable lithium batteries (or lithium-ion batteries) have been attracting much attention due to growing demands for electrical energy storage devices, in a wide variety of applications such as mobile phones or electric vehicles.[1][6] Because a large part of battery performance is determined by the electrode, intensive efforts have been devoted to explore new electrode materials in the past two decades. In the exploration process, several promising electrode materials have been found, such as spinel oxides ($\text{Li}_{4+x}\text{Ti}_5\text{O}_{12}$ [7][8] and $\text{Li}_{1-x}\text{Mn}_2\text{O}_4$ [9]) and phospho-olivine ($\text{Li}_{1-x}\text{FePO}_4$ [10][11][12][13][14]). They are now expected to be used in next-generation rechargeable lithium batteries.

The above mentioned materials commonly show a two-phase reaction upon Li insertion-extraction. One of the characteristics of two-phase insertion is the constant equilibrium potential over a wide composition range (See the explanation in Section 5.1). For example, in LiMn_2O_4 , a flat potential curve is observed during the charge-discharge process (Figure 3.1 (a)).

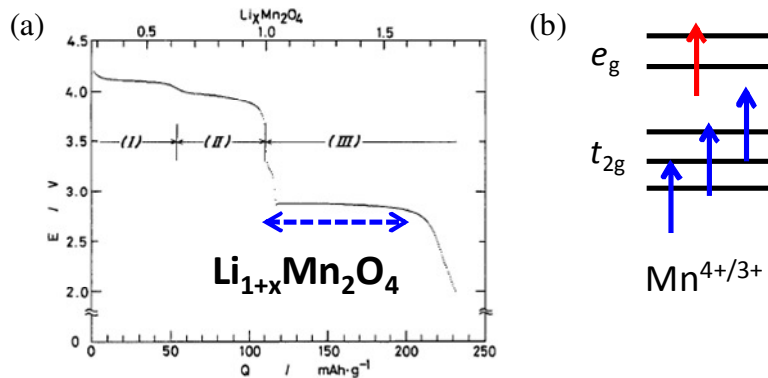


Figure 3.1 (a) An example of electrode materials ($\text{Li}_{1+x}\text{Mn}_2\text{O}_4$) showing a two-phase reaction on Li insertion. [9] (Dashed arrows indicate the constant voltage region.) (b) Electron transfer of high-spin $\text{Mn}^{4+/3+}$ in $\text{Li}_{1+x}\text{Mn}_2\text{O}_4$ (The electron from lithium enters the e_g orbital.)

The constant potential of a two-phase system should merit for practical applications

because the cell voltage does not decrease when the battery is in use. On the other hand, since the dynamics is largely dominated by the motion of domain boundaries between the two phases, two-phase systems often suffer from a slow charge-discharge rate and poor cycle performance. A discontinuous lattice strain at the phase boundary, which originates from the mismatch of lattice constants between the two coexisting phases, could be the most harmful kinetic barrier for Li-ion motion and induce fatigue of the lattice during cycling.

The so-called "zero-strain" material,[7] where the mismatch of lattice constants between phases is very small, is one of the ideal systems with a two-phase reaction, in which a low kinetic barrier and a small lattice strain at the phase boundary could be realized. If the strain energy at the interface between coexisting phases is reduced enough, the domain size, which characterizes the two-phase coexistence, could be smaller than the size of material particles.[15][16][17][18] In such a case, because Li ions can reach the domain boundary by intra-grain diffusion, domains would grow very rapidly. In fact, in the well-known "zero-strain" anode $\text{Li}_{4+x}\text{Ti}_5\text{O}_{12}$, one of the insertion materials with high rate capability,[19][20][21] a nanoscaled fine domain structure is reported in its two-phase state,[22] which is also discussed to be an important factor for the enhanced performance.[17]

3.2 How to design "zero-strain" materials - Suppression of the lattice distortion by itinerant t_{2g} orbitals

One of the major causes for the mismatch of lattice constants is the Jahn-Teller effect, which is typically observed in the 3 V region of $\text{Li}_{1+x}\text{Mn}_2\text{O}_4$ (the marked region in Figure 3.1 (a)) by high-spin Mn^{3+} (Figure 3.1 (b)). When a set of degenerate orbitals of transition metal ions are partially occupied by electrons during the charge-discharge process, surrounding ligands will distort to remove the degeneracy of orbitals so as the system can gain electronic energy. The Jahn-Teller effect in many cases occurs as a first order transition accompanied with a large lattice distortion, which is intimately linked to the two-phase reaction upon Li insertion-extraction.

What can be a good strategy for the suppression of the Jahn-Teller effect? For octahedral geometries of ligands as in spinel oxides, both t_{2g} and e_g orbitals can experience a Jahn-Teller effect associated with their orbital degeneracy, but the effect is much smaller for t_{2g} electrons than for e_g electrons because of the difference in

anisotropic charge distribution of orbitals with respect to ligand fields.[23] The itinerancy further reduces the degeneracy of bands and therefore suppresses the Jahn-Teller effect. We here propose that, considering reduction of the interfacial lattice strain in a two-phase state, itinerant t_{2g} electron systems (in which electrons only insert into or extract from t_{2g} orbitals) could be a possible candidate.

In this study, we report that spinel $\text{Li}_{1+x}\text{Rh}_2\text{O}_4$ satisfies the above requirements for a two-phase system. It is a cathode material with a flat operating potential of 3.2 V (vs. Li/Li^+) and shows a two-phase reaction. We found that the interfacial lattice strain between the two coexisting phases is much reduced, which is likely due to a suppressed Jahn-Teller effect. $\text{Li}_{1+x}\text{Rh}_2\text{O}_4$ can be regarded as a new "zero-strain" system.

3.3 A new "zero-strain" cathode material: LiRh_2O_4

LiRh_2O_4 crystallizes in the spinel structure,[24] one of the representative crystal structures of lithium battery electrodes.[7][8][9] Li and Rh ions occupy tetrahedral sites (8a) and octahedral sites (16d), respectively (Figure 3.2 (a)). LiRh_2O_4 contains 1 : 1 ratio of Rh^{3+} ($4d^6$) and Rh^{4+} ($4d^5$), both of which are in the low-spin state due to a large cubic crystal field and reduced Hund's coupling of $4d$ orbitals (Figure 3.2 (b)).

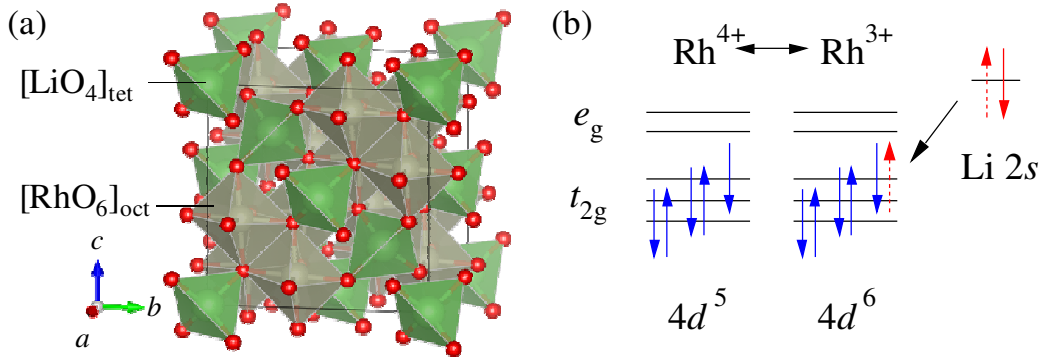


Figure 3.2 (a) The crystal structure of LiRh_2O_4 , containing $[\text{LiO}_4]$ tetrahedra and $[\text{RhO}_6]$ octahedra. (b) Electron transfer on discharging $\text{Li}_{1+x}\text{Rh}_2\text{O}_4$. Electrons flow from Li to t_{2g} orbitals of low-spin Rh ions.

Likely due to the broad $4d$ band as compared with $3d$, d electrons in LiRh_2O_4 should be itinerant in character. Indeed, LiRh_2O_4 is a paramagnetic metal at room temperature.[24] Reflecting those, although Rh^{4+} is a Jahn-Teller active ion in LiRh_2O_4 due to partially occupied t_{2g} orbitals, the Jahn-Teller transition is suppressed below room temperature,

230 K,[24] as compared to LiMn_2O_4 which exhibits the Jahn-Teller transition around 280 K.[25][26] $\text{Li}_{1+x}\text{Rh}_2\text{O}_4$ ($0 \leq x \leq 1$) with increasing Rh^{3+} in the Li insertion process should not largely suffer from the Jahn-Teller effect at room temperature, since LiRh_2O_4 ($x = 0$) contains the maximum concentration (50%) of Jahn-Teller active Rh^{4+} in the composition and Rh^{3+} is not a Jahn-Teller ion.

3.3.1 Sample preparation

LiRh_2O_4 was synthesized from Li_2O_2 and Rh_2O_3 by solid state reaction.[24] The raw materials were mixed and heated at 900 °C for 48 hours under an oxygen pressure of 5 atm. Structural characterizations of samples were carried out by powder X-ray diffraction. The diffraction results indicate that LiRh_2O_4 takes a cubic spinel structure ($a = 8.460(1) \text{ \AA}$) with a space group $Fd-3m$ (Figure 3.3 (a)). The synthesized sample was observed by SEM, showing that LiRh_2O_4 has a particle size around 10 μm (Figure 3.3 (b)).

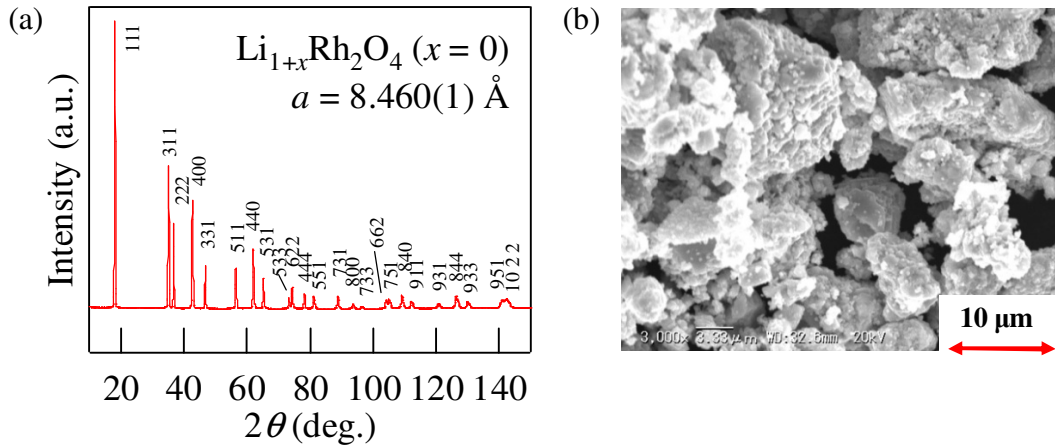


Figure 3.3 (a) X-ray diffraction patterns of synthesized LiRh_2O_4 . All the diffraction peaks are indexed in a spinel structure (space group $Fd-3m$). (b) The SEM image of LiRh_2O_4 . The particle size is around 10 μm .

Samples used for *ex situ* X-ray diffraction analysis, $\text{Li}_{1+x}\text{Rh}_2\text{O}_4$, were obtained by direct discharge from LiRh_2O_4 ($x = 0$) to each composition ($x = 0.2, 0.3, 0.4, 0.6, 0.8$ and 0.9). The discharged electrodes were sealed with polyethylene-nylon films in the glovebox before X-ray diffraction measurements.

3.3.2 Cathode performance of LiRh_2O_4

Electrochemical reactions of LiRh_2O_4 were investigated by inserting Li ions into and extracting from its structure. The cell voltage was initially charged to 4.8 V (vs Li/Li^+), and was then cycled between 4.8 V and 2.0 V. When Li ions are firstly extracted from LiRh_2O_4 , a single-phase reaction was observed, in which the slope of the potential curve varies with the Li composition (Figure 3.4), like the manganese spinel $\text{Li}_{1-x}\text{Mn}_2\text{O}_4$. The flat potential curve on further Li insertion implies a coexistence of two phases in the system, as observed in other spinel oxides such as $\text{Li}_{4+x}\text{Ti}_5\text{O}_{12}$ [7][8] and $\text{Li}_{1+x}\text{Mn}_2\text{O}_4$,[9]. This study has focused on the two-phase region of $\text{Li}_{1+x}\text{Rh}_2\text{O}_4$ ($0 < x < 1$).

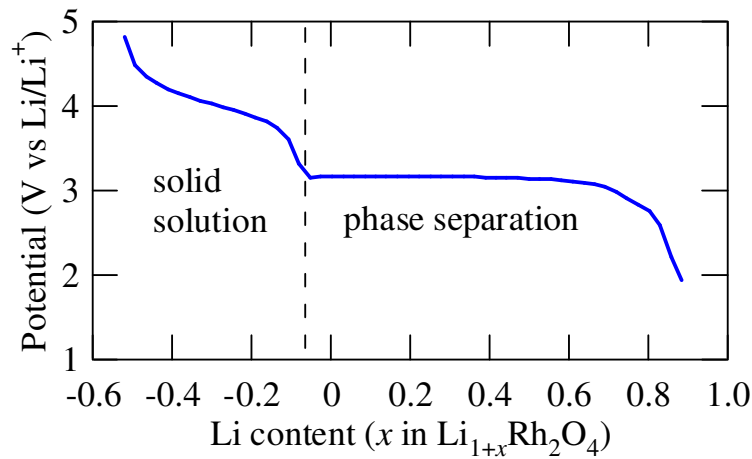


Figure 3.4 Electrochemical Li extraction and insertion for $\text{Li}_{1\pm x}\text{Rh}_2\text{O}_4$. (solid solution: $\text{Li}_{1-x}\text{Rh}_2\text{O}_4$; phase separation: $\text{Li}_{1+x}\text{Rh}_2\text{O}_4$)

The charge-discharge curve of $\text{Li}_{1+x}\text{Rh}_2\text{O}_4$ exhibits a flat potential curve around 3.2 V (vs. Li/Li^+), which is likely due to a coexistence of two phases (Figure 3.5 (a)). The flat potential curve appears over a wide composition range between $x = 0$ and $x = 0.8$. The cell voltage was initially charged to 4.5 V (vs Li/Li^+), and was then cycled between 4.5 V and 2.0 V at a 0.05 C rate (or at 5 mA/g). Rate capability was kept up to 0.5 C for present electrode samples. The specific capacity in the first cycle was *ca.* 90 mAh/g ($x = 0.9$), which corresponds to 90% of its theoretical capacity for $x = 1.0$ ($\text{Li}_2\text{Rh}_2\text{O}_4$), and was settled in *ca.* 80 mAh/g after 10 cycles (Figure 3.5 (b)). The fine reversibility implies that the discontinuous volume change of unit cells between coexisting two phases is rather small and the structural fatigue is suppressed.

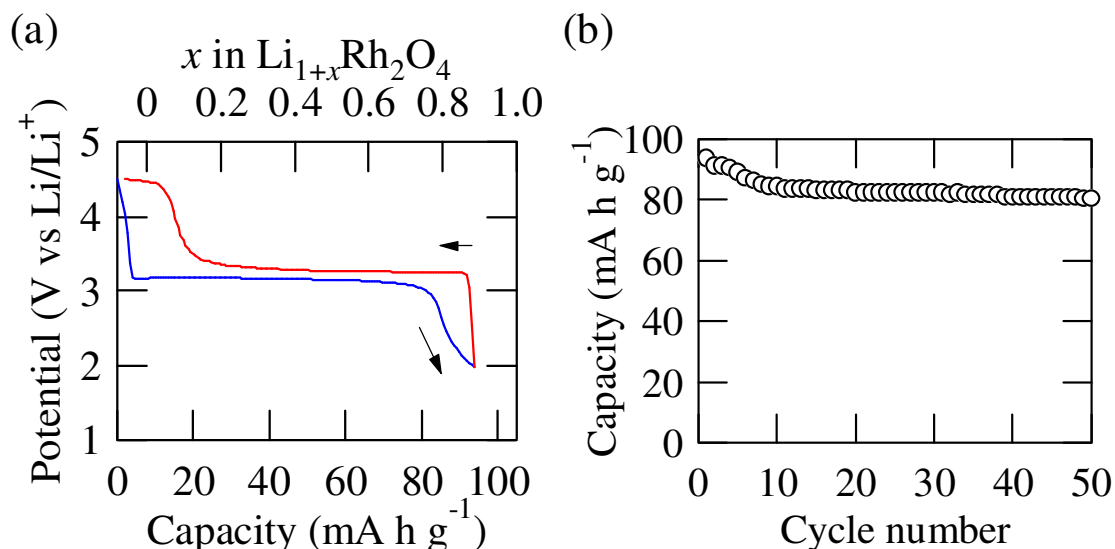


Figure 3.5 (a) The charge-discharge curve of $\text{Li}_{1+x}\text{Rh}_2\text{O}_4$ (the first cycle after initial charge). (b) Capacity retention of $\text{Li}_{1+x}\text{Rh}_2\text{O}_4$. The cell has been continuously cycled.

3.3.3 Evidence of the two-phase Li insertion in $\text{Li}_{1+x}\text{Rh}_2\text{O}_4$

Results of *ex situ* structural analysis evidenced the coexistence of two phases in the flat potential region. X-ray diffraction measurements were performed for selected compositions ($x = 0, 0.2, 0.3, 0.4, 0.6, 0.8$ and 0.9) (Figure 3.6 (a)). In the expanded view of diffraction patterns around 844 and 933 reflections within the composition range between $x = 0$ and $x = 0.8$ corresponding to the flat potential curve (Figure 3.6 (b-c)), peak profiles consist of the superposition of two peaks at $2\theta = 126.0^\circ, 126.3^\circ$ ($hkl = 844$) and $2\theta = 129.6^\circ, 130.0^\circ$ ($hkl = 933$), respectively. On the other hand, a single peak appears for the composition $x \geq 0.8$, where the potential curve shows slope, and the peak position shifts to a lower angle from $x = 0.8$ to 0.9 . From these results, it is clear that a two-phase coexisting state appears in the composition range with the flat potential curve, $0 \leq x < 0.8$, and a single-phase reaction occurs in the composition range with a sloped potential curve for $x \geq 0.8$.

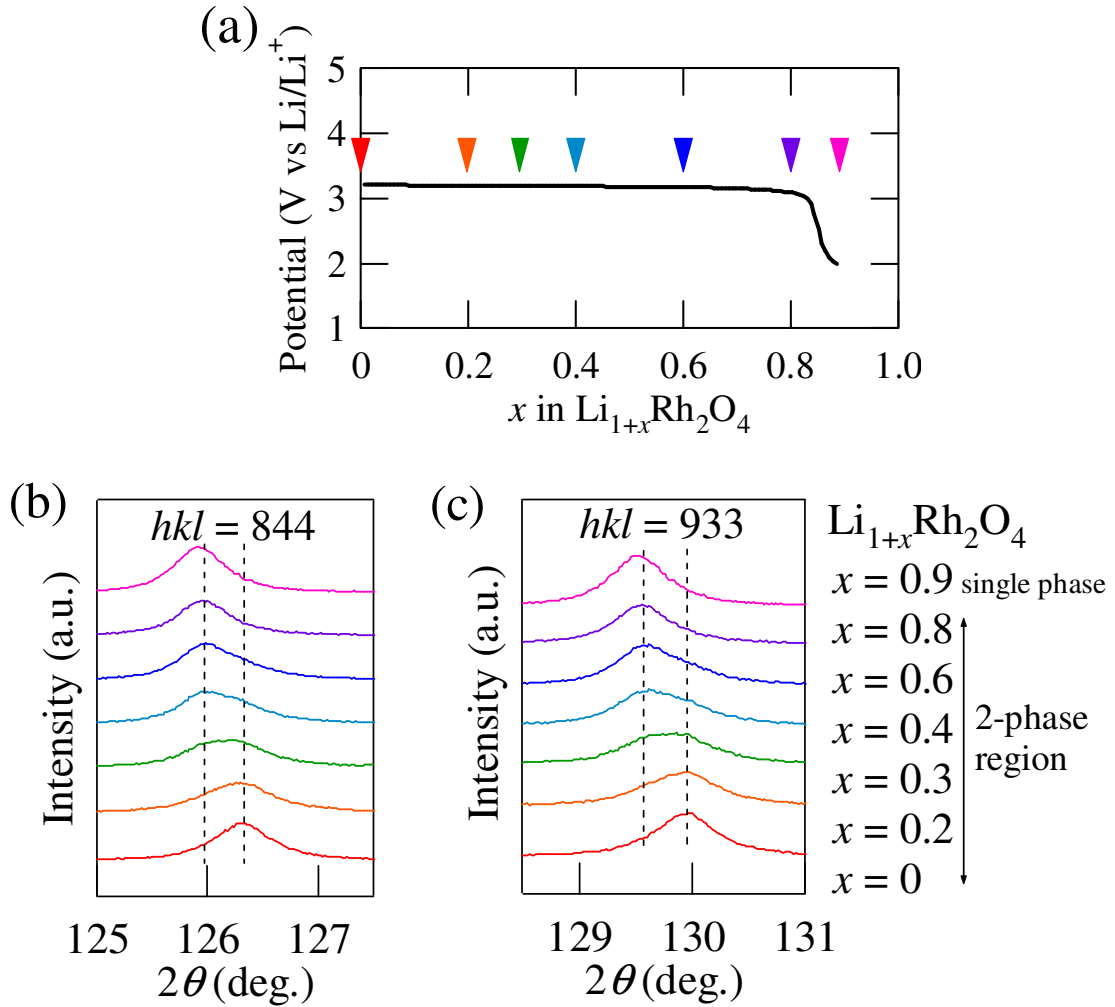


Figure 3.6 (a) The Li insertion process of $\text{Li}_{1+x}\text{Rh}_2\text{O}_4$ on discharge. Triangles indicate the compositions of discharged samples. (b-c) X-ray diffraction patterns of $\text{Li}_{1+x}\text{Rh}_2\text{O}_4$ with different x values. The diffraction peaks ($hkl = 844$ and 933) were measured with $\text{Cu } K\alpha_1$ radiation.

The open circuit potential (OCP) curve also confirmed the two-phase nature of $\text{Li}_{1+x}\text{Rh}_2\text{O}_4$. The cell was discharged for 3 h at a constant current density of 3 mA/g, and then the OCP was measured for 5 h. The OCP measurement was then repeated between discharging and resting. The obtained OCP clearly displays a flat potential curve (3.2 V vs Li/Li^+) over a wide range of the Li insertion process (Figure 3.7). According to the thermodynamic calculation of a two-phase equilibrium (Figure 5.1), the flat potential profile indicates the coexistence of two phases, which is also observed in other spinel oxides. [7][8][9]

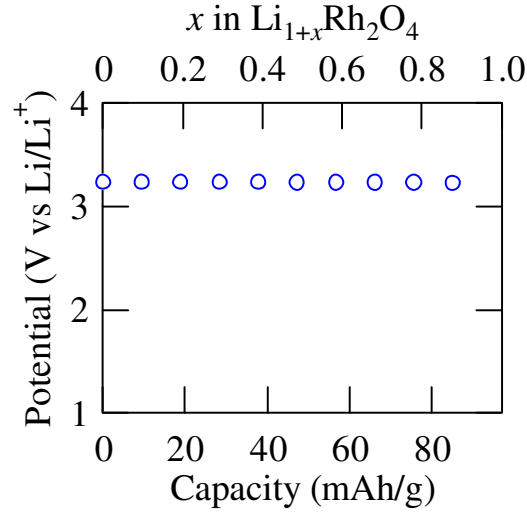


Figure 3.7 The open circuit potential curve of $\text{Li}_{1+x}\text{Rh}_2\text{O}_4$.

3.3.4 A small lattice distortion in $\text{Li}_{1+x}\text{Rh}_2\text{O}_4$ - The "zero-strain" behavior

Lattice parameters for the end members of LiRh_2O_4 and $\text{Li}_{1.8}\text{Rh}_2\text{O}_4$ are $a = 8.460(1) \text{ \AA}$ and $a = 8.475(6) \text{ \AA}$, respectively (Figure 3.8). The volume change of the unit cell is as small as *ca.* 0.5%, which is much smaller than other two-phase systems, such as $\text{Li}_{1+x}\text{Mn}_2\text{O}_4$ (*ca.* 5.6%)[9] and $\text{Li}_{1-x}\text{FePO}_4$ (*ca.* 6.8%),[10][13] and is comparable to $\text{Li}_{4+x}\text{Ti}_5\text{O}_{12}$ (*ca.* 0.2%), which is often called as a "zero-strain" material.[8]

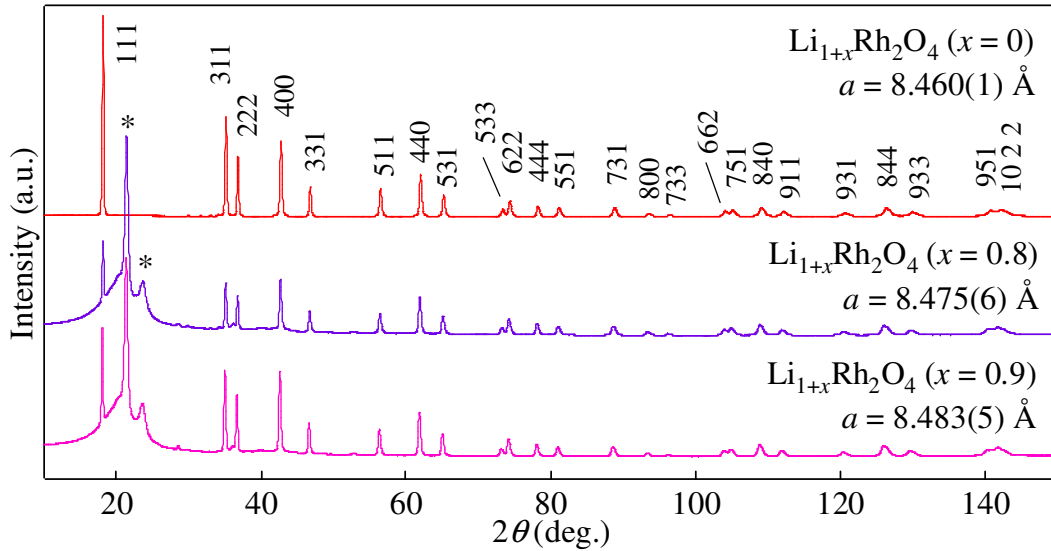
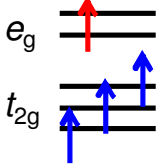


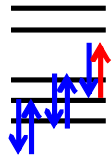


Figure 3.8 X-ray diffraction patterns of $\text{Li}_{1+x}\text{Rh}_2\text{O}_4$. The obtained structural parameters are given for each composition.

Taking into account that the lattice constant increases at $x \geq 0.8$ ($a = 8.483(5)$ Å for $\text{Li}_{1.9}\text{Rh}_2\text{O}_4$, Figure 3.8), the origin of the incomplete miscibility gap, which involves a small solid-solution compositional range $0.8 \leq x < 1$, could be attributed to a reduction in the lattice mismatch between the two coexisting phases.[12][27] In a two-phase system, the lattice strain induced by the difference of lattice parameters would decrease the energy gain due to the phase separation. In the case of $\text{Li}_{1+x}\text{Rh}_2\text{O}_4$, its lattice parameter increases when more Li ions are inserted into its structure at $x \geq 0.8$. Therefore, the miscibility gap of $\text{Li}_{1+x}\text{Rh}_2\text{O}_4$ does not span over the whole Li insertion but ends at $x = 0.8$.

The origin of this "zero-strain" behavior of $\text{Li}_{1+x}\text{Rh}_2\text{O}_4$ could be ascribed to the $4d$ electrons in t_{2g} orbitals with a moderated Jahn-Teller effect. By comparing the electronic structure of our model material $\text{Li}_{1+x}\text{Rh}_2\text{O}_4$ with other spinel oxides used in rechargeable lithium batteries (Table 3.1), it may be concluded from this study that systems with electrons transferring to itinerant t_{2g} orbitals will eventually suppress the volume change of electrode materials to a small value.

Table 3.1 Electron transfer and volume changes of spinel oxides on Li insertion.
(Red arrows indicate the electrons from lithium.)

Material	$\text{Li}_{1+x}\text{Mn}_2\text{O}_4$	$\text{Li}_{1+x}\text{V}_2\text{O}_4$	$\text{Li}_{4+x}\text{Ti}_5\text{O}_{12}$	$\text{Li}_{1+x}\text{Rh}_2\text{O}_4$
Redox couple	Mn 4+/3+	V 4+/3+	Ti 4+/3+	Rh 4+/3+
Electron transfer on Li insertion				
Volume change on Li insertion	5.6% ([9])	1.9% ([28])	0.2% ([8])	0.5% (This study)

The "zero-strain" behavior would lead to an ideal coexisting state, which shows little dependence on the particle size. To understand high rate capability in two-phase systems, it is indispensable to investigate the motion of phase boundaries. When an energy penalty at the interface induced by the lattice mismatch is relatively large, materials will form two phases inside one particle without any phase boundary below some specific particle size. [15][16][29] But in a "zero-strain" system, if the strain energy at the interface is suppressed enough, a phase boundary within one particle can be obtained regardless of the particle size. Such an ideal coexisting state could be visualized by

microscopic imaging techniques, like Transmission Electron Microscopy (TEM),[22] to reveal the nucleation process of the second phase and anisotropy of the phase boundary movement during domain growth.

In the representative "zero-strain" system $\text{Li}_{4+x}\text{Ti}_5\text{O}_{12}$, nanosized domains (*in which the formation of the phase boundary within single particles is necessary*) are proposed as a key enabler for its high rate capability. [17][18] It is suggested that abundant phase boundaries in a fine-domain structure and the shortened diffusion length of each domain (*which is necessary for Li ions to reach the interface between coexisting phases in the process of domain growth*) could contribute to the high rate capability.[15][16][17][18] If a coexistence state with nanosized domains is realized in $\text{Li}_{1+x}\text{Rh}_2\text{O}_4$ due to the same "zero-strain" character as proposed in $\text{Li}_{4+x}\text{Ti}_5\text{O}_{12}$, we might expect fast Li insertion-extraction to be observed.[19][21].

In the above cases, combining two "zero-strain" systems with two-phase reactions, LiRh_2O_4 and $\text{Li}_4\text{Ti}_5\text{O}_{12}$, a model lithium-ion battery could be realized. It should have an extremely flat potential, good cycle performance and high rate capability, since $\text{Li}_{1+x}\text{Rh}_2\text{O}_4$ and $\text{Li}_{4+x}\text{Ti}_5\text{O}_{12}$ can be regarded as the cathode (3.2 V vs. Li/Li^+) and anode (1.5 V vs. Li/Li^+) [7][8], respectively. Further investigation on the correlation between the coexisting domain state and rate capability in $\text{Li}_{1+x}\text{Rh}_2\text{O}_4$ might give a new insight for the dynamics of two-phase reactions in the Li insertion-extraction process.

In summary, $\text{Li}_{1+x}\text{Rh}_2\text{O}_4$ exhibits a two-phase reaction in the Li insertion-extraction process. A very small volume mismatch between the two phases, as small as that of the so-called "zero-strain" material, $\text{Li}_{4+x}\text{Ti}_5\text{O}_{12}$, has been found, which is highly likely induced by itinerant $4d$ electrons in the t_{2g} orbitals with a suppressed Jahn-Teller effect. $\text{Li}_{1+x}\text{Rh}_2\text{O}_4$ could be regarded as a new "zero-strain" material with a two-phase reaction. We propose t_{2g} and itinerant character of d electrons involved in the reaction process as one of the strategies to design "zero-strain" systems with a two-phase reaction.

Chapter 4: Cathode materials for rechargeable magnesium batteries

4 Cathode materials for rechargeable magnesium batteries

4.1 Motivation - Magnesium batteries as an alternative to lithium

Light and powerful rechargeable lithium batteries have made portable electronic devices and electric vehicles possible in our lives. But lithium is expensive and costs too much with still limited energy density in practical applications.[30][31][32] Meanwhile, reliability and safety of lithium batteries are always being concerned because lithium is a highly reactive metal. The presence of both combustible (lithium, organic electrolyte) and oxidizing materials (cathode) in a battery cell carries a risk of runaway reactions, which has caused fire and explosion accidents thus may hinder further applications of lithium batteries.[33][34][35] Instead, conventional lead-acid and Ni-Cd batteries are still being used in many fields as power supplies. Nowadays since the issues of energy storage and power shortage are receiving more and more attention, "green" batteries are expected to be developed and take place in the future - they are supposed to be environmentally friendly with high performance but low cost.

Magnesium batteries are designated to replace lead-acid and Ni-Cd batteries,[36] providing a more energy-dense, low-cost and eco-friendly energy storage system, especially in large load applications like electric vehicles. Magnesium has similar chemical properties to lithium such as ionic radii (0.062 nm for Mg, 0.068 nm for Li) and electrode potentials (-2.37 V for Mg, -3.03 V for Li, vs SHE). However, magnesium promises to be safer and cheaper than lithium: magnesium is stable in the atmosphere and has a much higher natural abundance in the earth's crust (1.93% for Mg, 0.006% for Li, from Clarke numbers [37]). Furthermore, magnesium batteries potentially have a higher storage capacity than lithium ones, because electrochemical reactions of Mg ions involve two electrons rather than one for Li ions.

4.2 Difficulties in making rechargeable magnesium batteries

All of the advantages are already fascinating enough to attract researchers working on rechargeable magnesium batteries, based the same insertion principle as in rechargeable lithium batteries. However, magnesium batteries have not yet been developed practically, and it is much more difficult to construct a functional magnesium battery

compared to lithium because:

- (1) The magnesium metal anode becomes inactive in most electrolytes (Section 4.2.1).
- (2) Strong Coulomb interactions make most materials unable to reversibly host Mg ions due to the slow Mg^{2+} diffusion kinetics (Section 4.2.2).
- (3) Only a few studies have been conducted so far and most of them achieved poor electrode performance (Section 4.2.3).

Too many barriers are on our way to enter the field of magnesium batteries. Nevertheless, in order to find possible candidate materials, all these problems must be overcome in this study (Section 4.3).

4.2.1 Magnesium metal is inactive in most conventional electrolytes

Magnesium tends to develop passivation "blocking" layers at its surface, which are the results that magnesium reacts with O_2 , H_2O and CO_2 in the atmosphere (Figure 4.1). Even polished in an argon-filled glovebox, magnesium metal is still covered with dense layers consisting of mainly $\text{Mg}(\text{OH})_2$. [38]

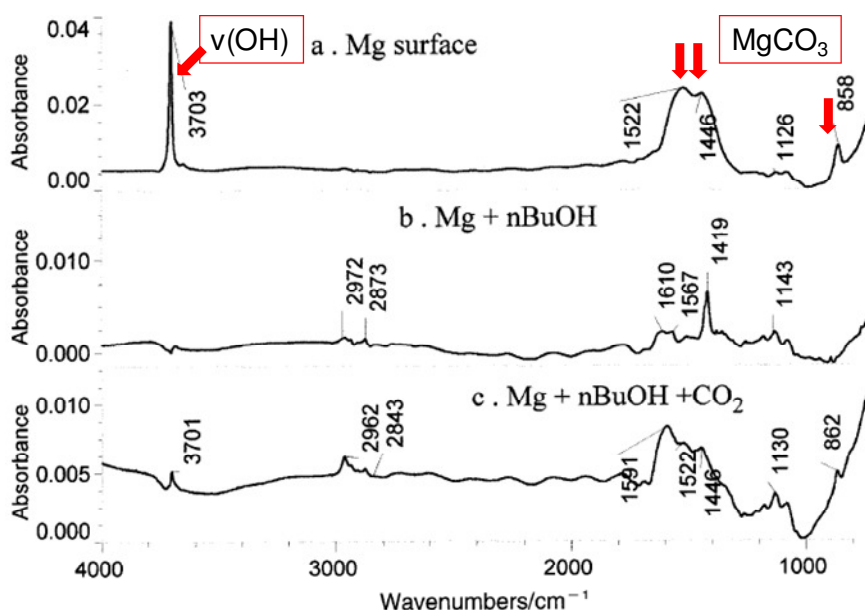


Figure 4.1 FTIR spectra of the magnesium metal's surface: (a) reacts with H_2O and CO_2 ; (b) cleaned and reacts with n-butanol; (c) reacts with CO_2 after (b). [38]

Unlike the Li-ion conducting "passivation" layers at the surface of lithium battery anodes, the passivation layers of magnesium do not conduct Mg ions in most conventional electrolytes. [38] Since the passivation layers can effectively block Mg

ions from passing through, the magnesium metal anode cannot function as a reversible electrode for Mg deposition and dissolution (Figure 4.2). Therefore conventional magnesium electrolytes analogous to lithium ones (like $\text{Mg}(\text{ClO}_4)_2$) are incompatible with the magnesium anode.

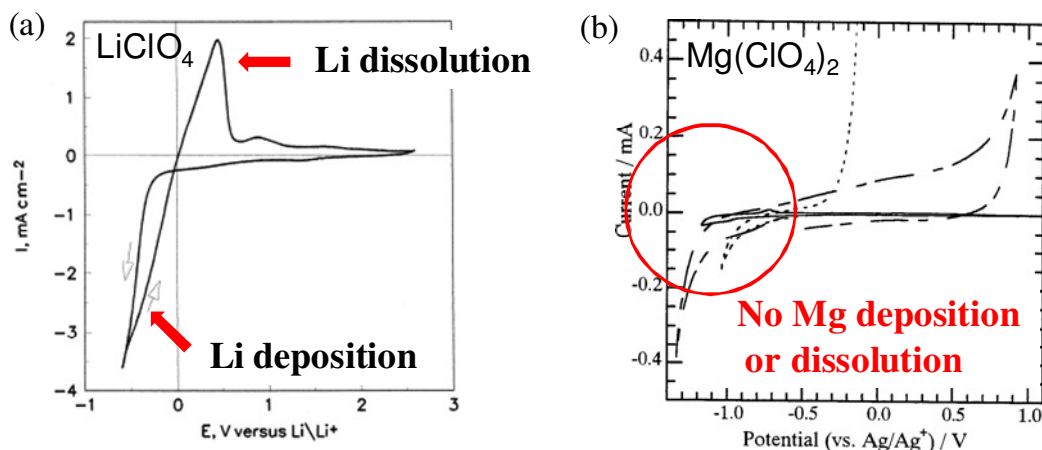


Figure 4.2 Cyclic voltammograms of: (a) the LiClO_4 electrolyte showing reversible Li deposition and dissolution;^[39] (b) the $\text{Mg}(\text{ClO}_4)_2$ electrolyte showing no reversibility of Mg deposition or dissolution.^[40]

For example, our study has tested a compound V_2O_5 , which has been widely studied as a cathode material of lithium batteries. Under the similar conditions to lithium battery cells,^[40] our magnesium cell could not work at all: only a very small discharge capacity was observed without any reversibility (Figure 4.3). Because the cell voltage (*cathode potential vs anode potential*) cannot be properly measured due to the unsteady magnesium anode potential in $\text{Mg}(\text{ClO}_4)_2$, reversible charge-discharge reactions are impossible unless using a third electrode as the potential reference.

In a three-electrode electrochemical cell (described in Section 2.2), the Mg^{2+} supply is from the $\text{Mg}(\text{ClO}_4)_2$ electrolyte solution since the magnesium anode remains inactive. Although the three-electrode cell allows us to screen possible candidate materials for magnesium batteries, new electrolytes compatible with magnesium metal need to be introduced.

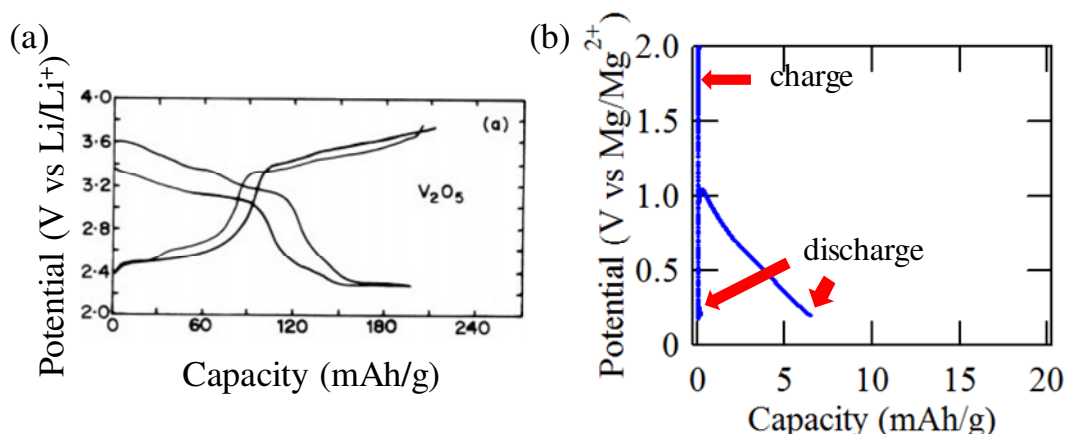


Figure 4.3 Typical charge-discharge curves of electrochemical cells using V_2O_5 as the cathode material: (a) anode: lithium metal; electrolyte: $LiClO_4$ (1 M) in ethylene carbonate-dimethyl carbonate;[41] (b) anode: magnesium metal; electrolyte: $Mg(ClO_4)_2$ (1 M) in acetonitrile (this study).

Reversible Mg deposition and dissolution could occur in alkyl- or aryl-magnesium halides, or called Grignard reagents, with a general formula $RMgX$ (R for alkyl or aryl, X for halogen elements, Figure 4.4 (a-b)).[36][38] Based on the Grignard reagents, a magnesium electrolyte using magnesium organohaloaluminate salts, like $Mg(AlCl_2EtBu)_2$, has been reported as an electrochemically reversible electrolyte for magnesium batteries (Figure 4.4 (c)).[36] The new electrolyte prevents a magnesium anode from becoming inactive thus allows investigating for new cathode materials.

However, the $Mg(AlCl_2EtBu)_2$ electrolyte has a relatively narrow electrochemical window (0 ~ 2.2 V vs Mg/Mg^{2+}),[36][44][45][46][47] compared to the conventional electrolyte $Mg(ClO_4)_2$ (0 ~ 4 V vs Mg/Mg^{2+}).[38][48] (*Within the potential window there is no decomposition of the electrolyte.*) Our study has confirmed that no decomposition of the electrolyte was observed up to 2 V vs Mg/Mg^{2+} under present experimental conditions (Figure 4.5). It limits us to search for materials with low operating potentials so as to fit in the electrochemical window of $Mg(AlCl_2EtBu)_2$.

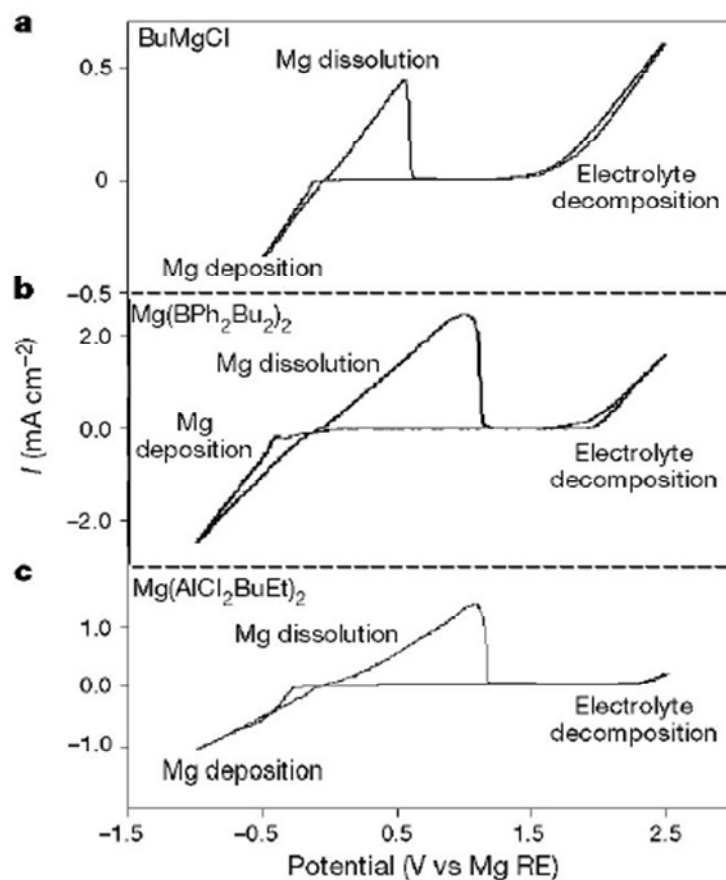


Figure 4.4 Cyclic voltammograms of electrolyte solutions in which magnesium can be deposited reversibly. (RE: reference electrode) [36]

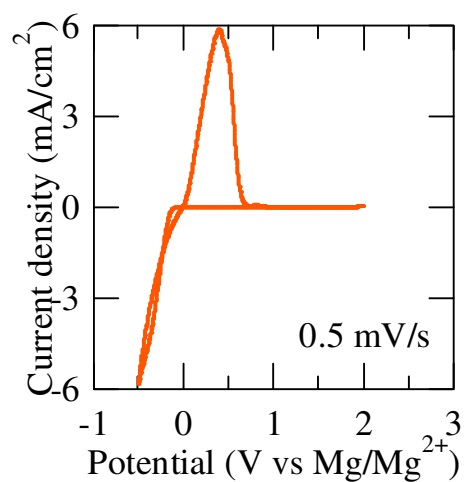


Figure 4.5 Mg deposition and dissolution in $\text{Mg}(\text{AlCl}_2\text{EtBu})_2$ (0.25 M dissolved in tetrahydrofuran; working electrode: Cu; counter and reference electrode: Mg)

4.2.2 Cathode irreversibility by strong Coulomb interactions from Mg ions

It is discussed that charge redistribution of a multivalent cation like Mg^{2+} , would cause slow diffusion kinetics due to strong Coulomb interactions existing between Mg ions and the local crystal structure.[42][43] As a result, Mg ions can be easily trapped in the lattice of electrode materials (Figure 4.6), which irreversibly shuts down the cathode performance of magnesium batteries.

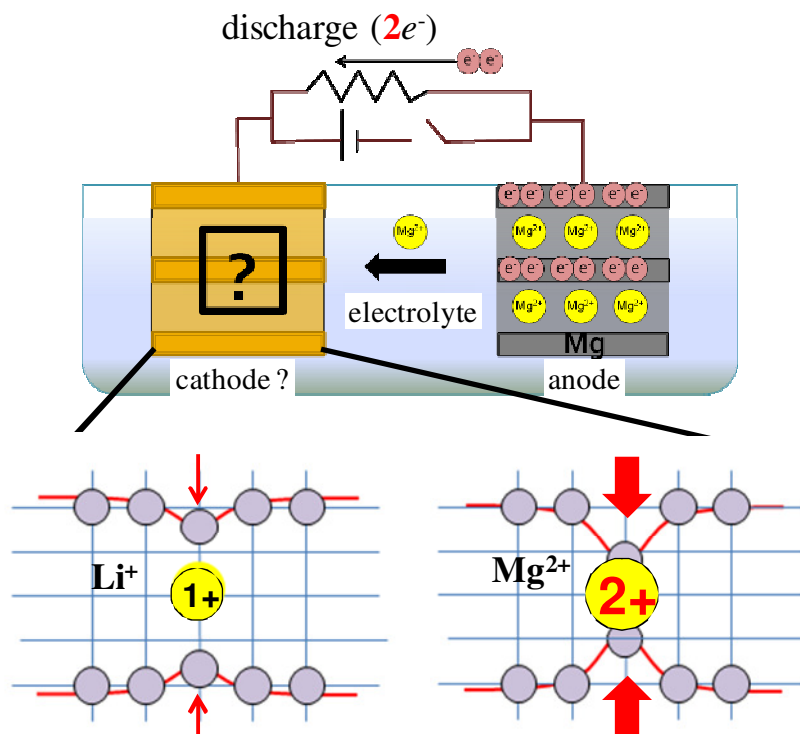


Figure 4.6 Schematic illustrations of Coulomb interactions between guest ions and the local crystal structure in batteries during discharge. Mg ions are easily trapped in the lattice due to the positive charge of two rather than one for Li ions.

4.2.3 Most approaches so far only achieved poor cathode performance

Until now only a few studies of magnesium batteries have been conducted, because researchers prefer not to choose magnesium batteries with so many hurdles in both chemistry and physics. Meanwhile, material research of magnesium batteries has followed the same idea as in lithium batteries that searching for host materials with available void spaces for Mg ions in their structures.

However, due to the slow and easily trapped Mg^{2+} kinetic behaviors discussed previously, most studies concluded that electrode materials used in lithium batteries failed to reversibly host Mg ions, but only displayed poor cathode performance. For example, preliminary studies by P. Novak *et al* and other research groups showed that Mg ions were difficult to be inserted into even simple structure compounds such as V_2O_5 , TiS_2 , ZrS_2 , RuO_2 , Co_3O_4 , [49] and $\text{Mg}_x\text{Ti}_2(\text{PO}_4)_3$. [50]

In recent reports, a common way to improve Mg^{2+} kinetics is to decrease the particle size of electrodes, by milling or low-temperature synthesis of nanoscaled materials. [40][51][52][53] A smaller particle size shortens the diffusion length for ions and forces them to access from the electrolyte to available sites of void spaces in the host structure. However, it is quite possible that a high surface area of materials enhances the chance of undesirable side reactions with the electrolyte and reduces the packing density of electrodes at the mean time.

Some studies also suggest that Mg insertion kinetics could be improved if other anions or molecule groups coinsert into the host structure, because additional ionic groups around Mg ions might shield its bivalent charge character. For example, water is added to vanadium or molybdenum oxides to improve their electrochemical behaviors, [49][54][55] but the drawbacks are obviously destructive: (1) big H_2O molecules will cause local deformations of the host structure and decrease the maximum insertion level of the electrode capacity; (2) the "wet" electrolyte should be dangerous because it may react with the metallic magnesium anode.

4.3 Strategies in this study - Design materials focusing on the electronic picture

In order to overcome those barriers on the way to magnesium batteries (Section 4.2), it is necessary to go back to the fundamental aspect of materials science and switch our guideline of material research from investigating crystal structures to the electronic aspect of electrode materials. Our original ideas are based on the physics and chemistry of a reported reversible magnesium insertion material (Section 4.3.1) as well as successful lithium battery electrodes (Section 4.3.2). Exploration of new candidate materials for magnesium batteries has been carried out (Section 4.3.3) in this work.

4.3.1 Cluster structures moderate the drastic valance change on Mg insertion

The most representative material in which reversible Mg insertion has been achieved is Mo_6S_8 , with a typical specific capacity *ca.* 75 mAh/g and a cycle life over 500 cycles (Figure 4.4),[36] which is reported by D. Aurbach *et al*, using the reversible $\text{Mg}(\text{AlCl}_2\text{EtBu})_2$ electrolyte which is also developed by the same research group. The crystal structure of Mo_6S_8 may be considered as a stacking of $[\text{Mo}_6\text{S}_8]$ blocks containing octahedral $[\text{Mo}_6]$ clusters inside cubes of sulfur atoms (Figure 4.4). Guest Mg ions are located at two sites (inner and outer rings) between the blocks.

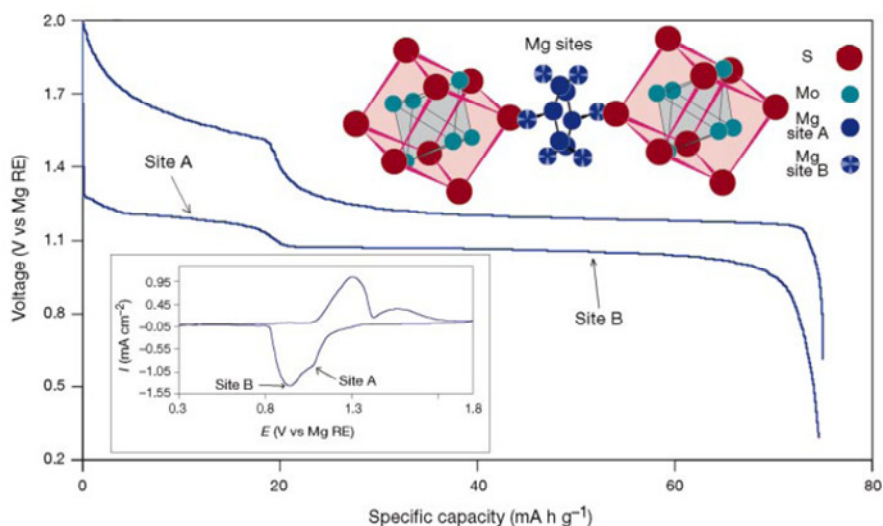


Figure 4.7 Typical electrochemical behavior and the crystal structure of $\text{Mg}_x\text{Mo}_6\text{S}_8$. (inset: the cyclic voltammogram of a steady Mg insertion-deinsertion cycle) [36]

In Mo_6S_8 , the electronic charge can easily redistribute on Mg insertion because of its special cluster structure.[42] $[\text{Mo}_6]$ clusters exchange electrons as a whole unit, but the valance state of each Mo only changes slightly ($2e^-$ for $[\text{Mo}_6]$, $2/6 e^-$ for Mo, per one Mg^{2+}). These metal clusters moderate the drastic valance change on Mg insertion and assist the charge redistribution to form electrical neutrality in the local structure.[43]

The feasibility of cluster compounds for magnesium batteries has been tested in this work. A well-known cluster molecule, C_{60} , was tested as the cathode material in a three-electrode cell (as described in Section 2.2). As expected, the giant C_{60} cluster

simply shows reversible charge-discharge reactions (Figure 4.8 (a)). Although the obtained specific capacity is still small compared to Mo_6S_8 (Figure 4.8 (b)), it implies that the cluster structure may potentially host Mg ions after all.

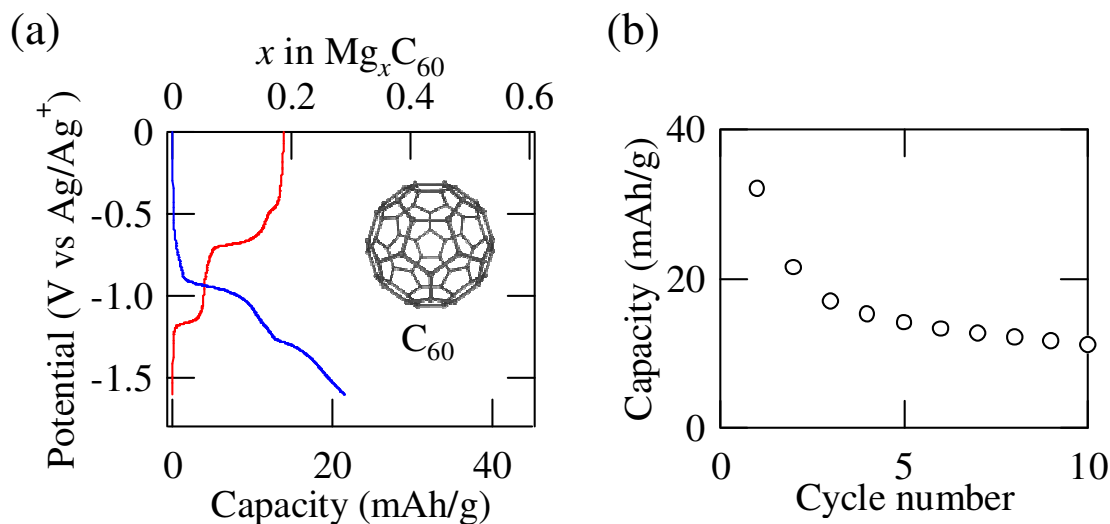


Figure 4.8 (a) Charge-discharge curves of Mg/C_{60} (the second cycle, Ag/AgNO_3 is used as the reference electrode). (b) Capacity retention of Mg/C_{60} . The cell has been continuously cycled.

Other cluster compounds studied by our group also revealed reversible Mg insertion reactions.[56] It appears that compounds with cluster structures seem to be unique candidates for electrode materials, but the number of these compounds is limited. We need to find other alternate materials that have a similar electronic environment to assist the redistribution of additional bivalent charge on Mg insertion.

4.3.2 Use hybridized d - p orbitals to create "electronic cluster" structures

The two electrons during Mg insertion induce a drastic valence change at the transition metal site, but the valence change might be relaxed by electron compensation from ligand anions, only if energy levels of d (metal) and p (anion) orbitals are close to each other. In a system with weakly hybridized d and p orbitals, d characterized molecular orbitals still dominate the electron transfer on Mg insertion; in other words, electrons go to transition metal atoms only (left scheme in Figure 4.9). But in a strongly hybridized system, electrons could be accepted by d - p characterized molecular orbitals formed via hybridization of d and p orbitals (right scheme in Figure 4.9). Extended polyhedra of a

central metal atom and surrounding anions can exchange electrons like "electronic clusters". Therefore materials with strongly hybridized d and p orbitals might be a potential system to moderate the valance change on Mg insertion.

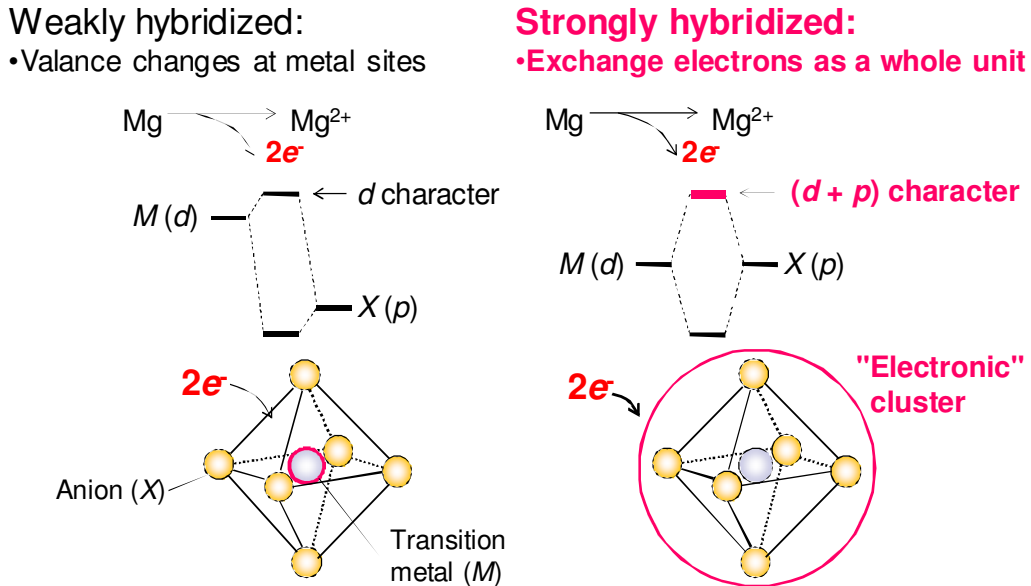


Figure 4.9 Schematic illustrations of the d - p orbital hybridization affecting behaviors of ligands during the "insertion" of electrons. In a strongly hybridized case each polyhedron exchanges electrons as a whole unit like metal clusters.

Actually, if we focus on the energy level difference between d and p orbitals in reported electrode materials, examples of d - p hybridized systems can be easily found among successful ones (circled elements in Figure 4.10): the first reported lithium intercalation material TiS₂, the first commercialized cathode material MoS₂, widely used cathode materials LiCoO₂, LiMn₂O₄ and LiFePO₄, and even the unique cluster compound for magnesium batteries Mo₆S₈. All of these practically succeeded examples imply the feasibility of our d - p hybridization idea.

Hybridization of d and p orbitals has been discussed for lithium battery electrodes LiMO₂. Calculated results of electron compensation from oxygen ligands indicate that upon Li intercalation, oxygen dominates the charge transfer process especially in the compounds of late transition metals.[59] These results are consistent with the physical fact that late transition metals have close orbital energy levels between their d orbitals and oxygen's p orbital (Figure 4.10).

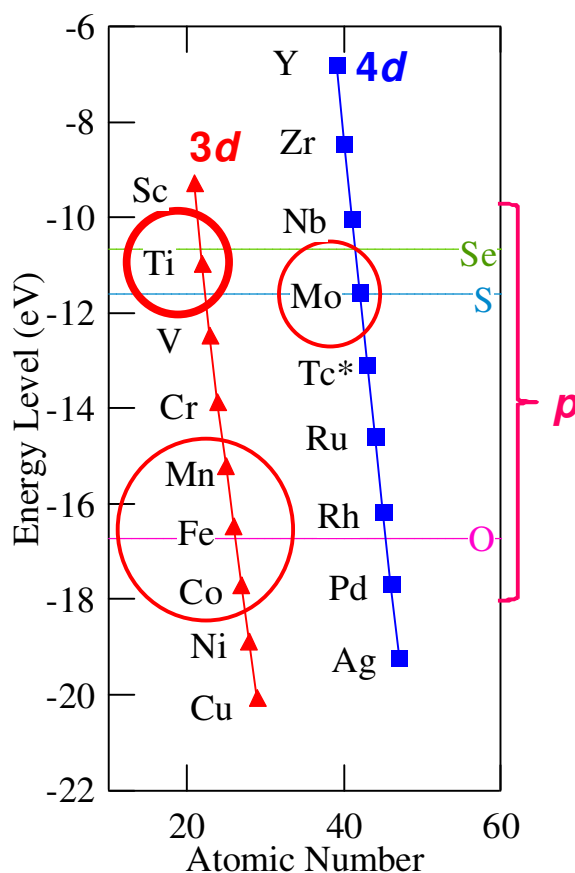


Figure 4.10 Orbital energy levels for 3d and 4d transition metals (3d and 4d orbitals) and oxygen 2p, sulfur 3p, selenium 4p orbitals. [57][58]

4.3.3 Candidate materials proposed with strong *d-p* orbital hybridization

From the calculated orbital energy levels (Figure 4.10), elements with close *d* and *p* orbitals can be divided into two groups: early transition metals with sulfur or selenium; late transition metals with oxygen. Compounds consisting of elements in each group should have strongly hybridized *d* and *p* orbitals.

However, the relatively narrow electrochemical window of the $\text{Mg}(\text{AlCl}_2\text{EtBu})_2$ electrolyte used in this study is another important factor that limits our choices of materials to those having low operating potentials (Section 4.2.1). The operating potential at which Mg insertion happens depends mainly on the energy level of *d* orbitals (Section 1.3.1), thus higher *d* energy levels would result in a low electrode potential since the difference of Fermi levels between magnesium and transition metal becomes smaller.

Titanium has been chosen for the transition metal in our candidate materials to satisfy the requirements discussed above:

- (1) The $3d$ energy level of titanium is very close to p orbitals of sulfur or selenium.
- (2) Titanium's $3d$ orbital has a relatively high energy level (for a low operating potential).

Besides, titanium also meets the needs for low cost materials, since it is the second most abundant element among transition metals.[37]

We here propose two candidate materials for magnesium batteries, TiSe_2 and TiS_3 . Both compounds have showed promising performance as magnesium battery cathodes, including reversible charge-discharge reactions with higher or comparable specific capacities to Mo_6S_8 . Hybridized d - p systems would be a clear guideline for exploring electrode materials of magnesium batteries and even other multivalent-ion batteries that depend strongly on the electronic structure of electrodes.

4.4 Magnesium battery cathode material: TiSe_2

TiSe_2 has a layered structure with $[\text{TiSe}_6]$ octahedra forming slabs in the ab plane, and the $[\text{TiSe}_2]$ slabs stack along the c axis by van der Waals force (Figure 4.11).

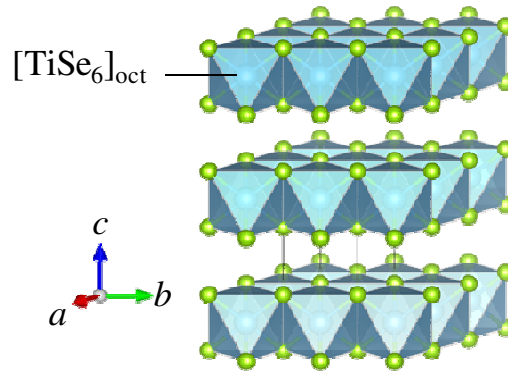


Figure 4.11 The crystal structure of TiSe_2 , consisting of $[\text{TiSe}_6]$ octahedra forming slabs that stack along the c direction.

The calculated band structure of TiSe_2 shows metallic conductivity (Figure 4.12), which is favorable for electrode applications. From its DOS structure hybridized d and p orbitals could be observed near the Fermi energy level (Figure 4.13), where the electron transfer on Mg insertion might be assisted as discussed previously.

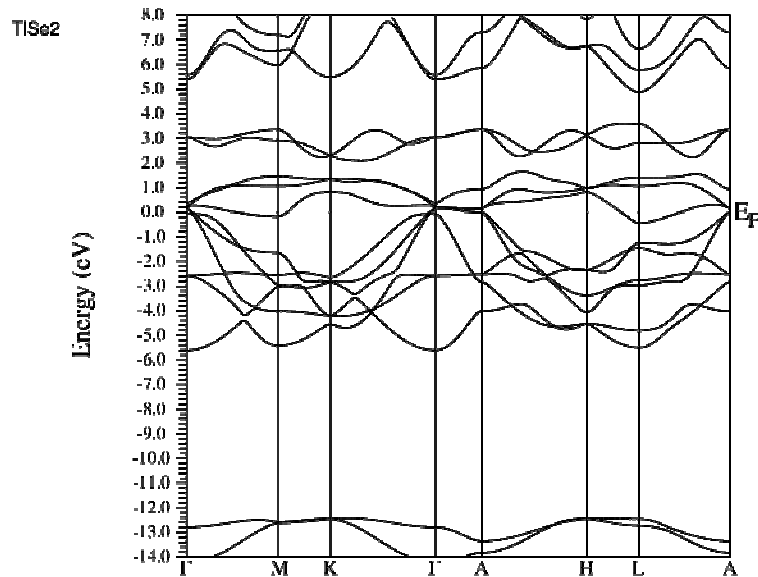


Figure 4.12 The band structure of TiSe_2 .

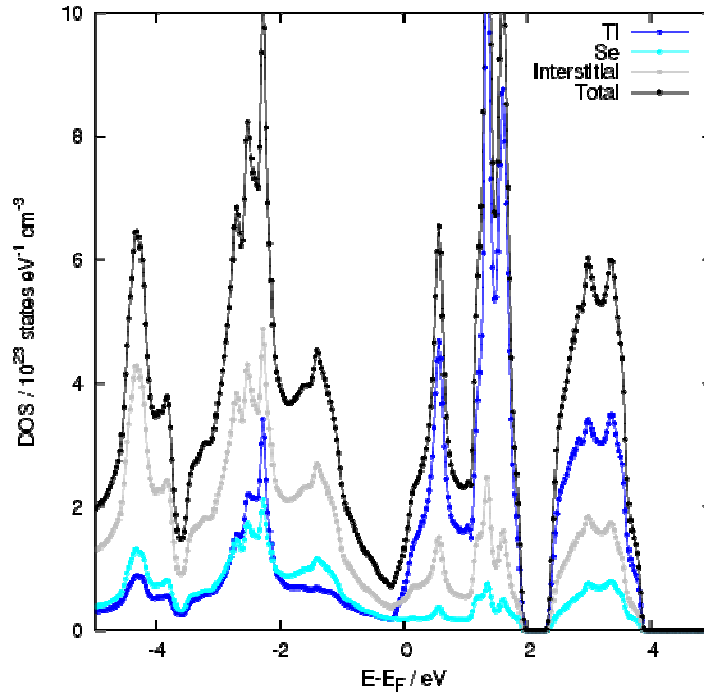


Figure 4.13 Calculated DOS of TiSe_2 .

TiSe_2 (> 99%, powder) was purchased from High Purity Chemicals. The TiSe_2 sample shows a layered structure with a space group $P-3m1$ (Figure 4.14). The difference in peak intensities between experimental and reference data is due to orientation of its layered crystal structure, which could not be eliminated by our laboratory X-ray diffraction measurements.

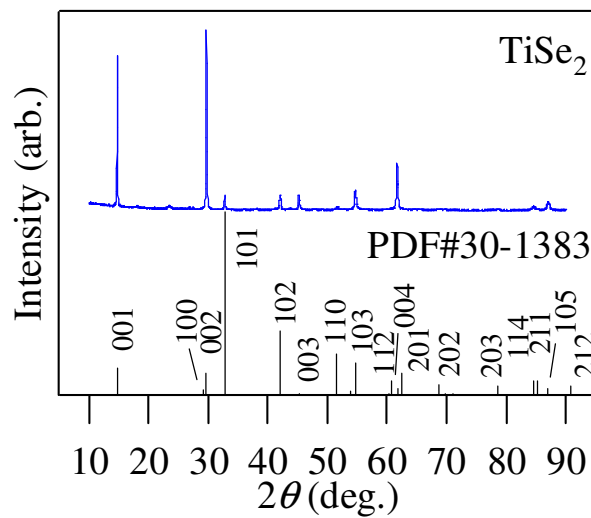


Figure 4.14 X-ray diffraction patterns of the TiSe_2 sample and reference data.

4.4.1 Reversible charge-discharge reactions in Mg/TiSe₂

Electrochemical charge and discharge curves of Mg/TiSe₂ cells indicate a specific capacity over 100 mAh/g (Figure 4.15 (a)), which is larger than the reported Mg/Mo₆S₈ system (*ca.* 75 mAh/g). The operating potential is about 1 V (vs Mg/Mg²⁺), which is as low as expected for such an early transition metal. Charge and discharge cycling was repeated reversibly over 50 cycles (Figure 4.15 (b)).

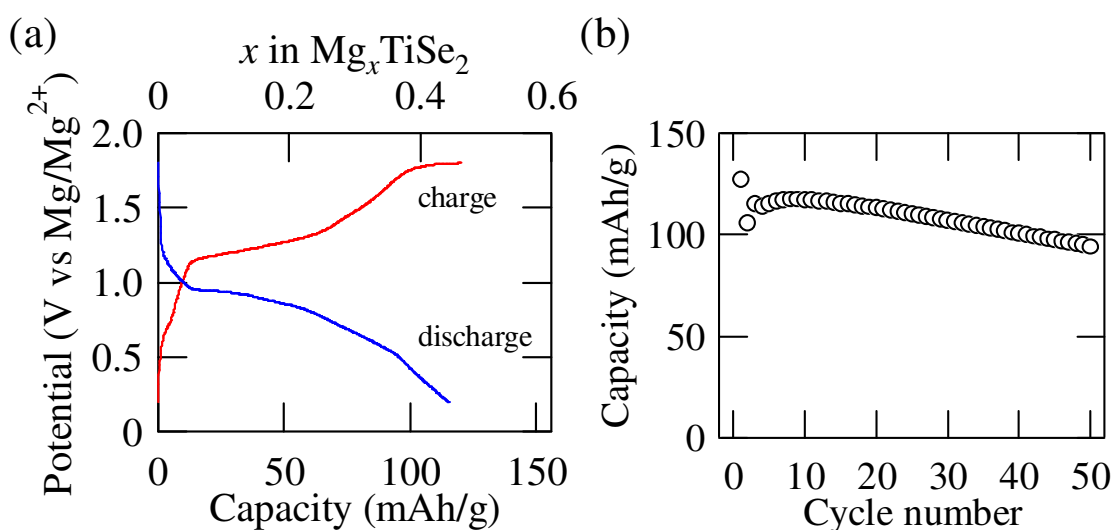


Figure 4.15 (a) Charge-discharge curves of Mg_xTiSe₂ (the second cycle). (b) Capacity retention of Mg_xTiSe₂. The cell has been continuously cycled at 5 mA/g.

Mg/TiSe₂ cells have been tested at various discharge rates (Figure 4.16). Mg_xTiSe₂ keeps *ca.* 50% of its discharge capacity at a high current density of 50 mA/g. If the theoretical insertion capacity of Mg_xTiSe₂ is estimated to $x = 0.5$, which is the same insertion level for Li_xTiS₂ based on the valance change, [60] a 50 mA/g current density could be converted to a 0.4 C rate.

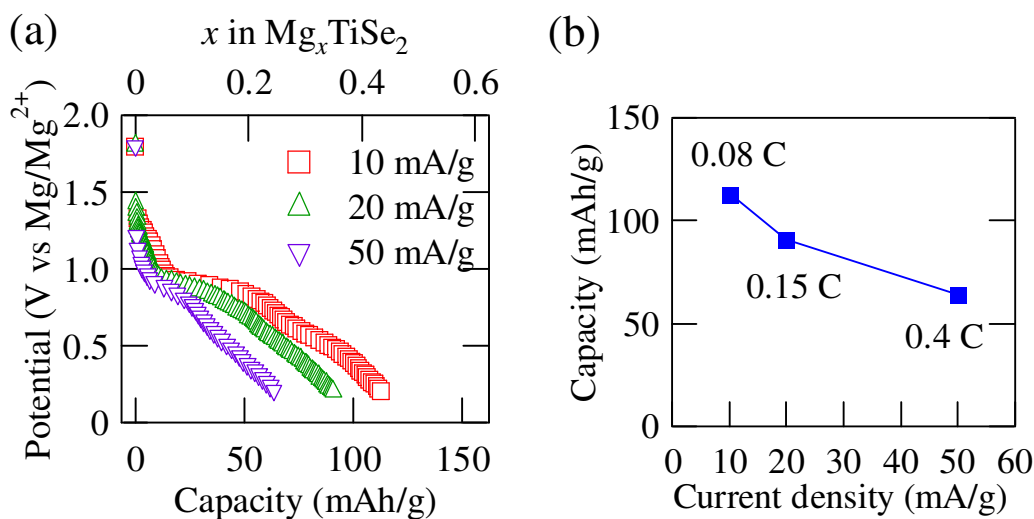


Figure 4.16 (a) Discharge curves and (b) capacity retention of Mg_xTiSe_2 at different current densities. The C rate is based on a theoretical specific capacity of 130 mAh/g ($\text{Mg}_{0.5}\text{TiSe}_2$).

4.4.2 Reversible changes of structural parameters in Mg_xTiSe_2

Two sets of electrochemically discharged and charged Mg_xTiSe_2 electrodes were prepared for *ex situ* structural analysis: one set samples were sealed with polyethylene-nylon films in the glovebox before X-ray diffraction measurements; the other set used for preliminary study was measured by X-ray diffraction immediately after being transferred out of the glovebox.

Preliminary *ex situ* structural measurements of discharged electrodes shows that Mg_xTiSe_2 keeps its original layered TiSe_2 structure in the charge-discharge process (Figure 4.17 (a)), with the lattice expanding along *a* and *c* axes (Figure 4.17 (b-c)).

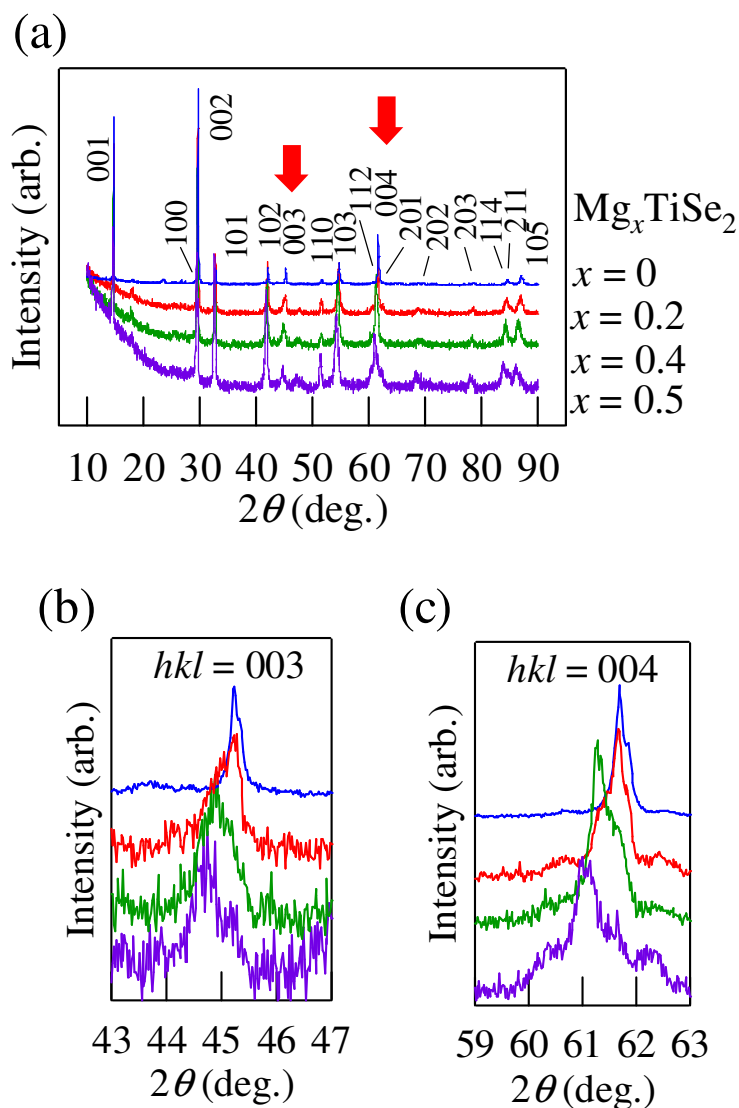


Figure 4.17 (a) X-ray diffraction patterns of Mg_xTiSe_2 electrodes with different x values. (b) Expanded view of the 003 reflection (marked by arrow in the figure (a)). (c) Expanded view of the 004 reflection (marked by arrow in the figure (a)).

To examine whether the lattice expansion is reversible during charge and discharge reactions, Mg_xTiSe_2 electrodes in both charged and discharged states were examined by X-ray diffraction. It could be clearly seen that the diffraction peak ($hkl = 004$) shifts back in the charged electrode (Figure 4.18).

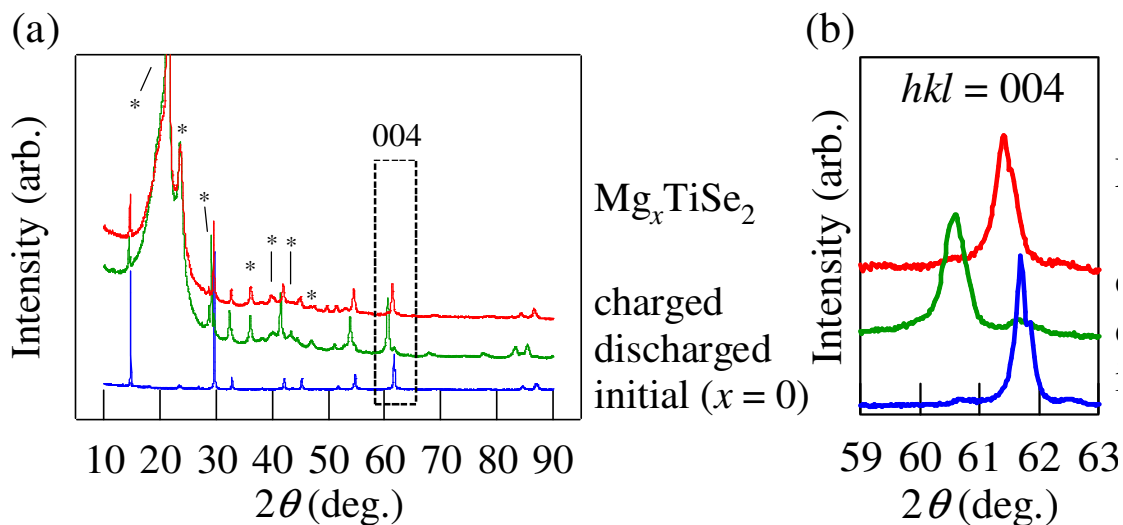


Figure 4.18 (a) X-ray diffraction patterns of initial, discharged and charged Mg_xTiSe_2 electrodes. The discharged and charged samples were sealed with polyethylene-nylon films (asterisks in the diffraction patterns) in an argon-filled glovebox. (b) Expanded view of the $hkl = 004$ reflection.

Structural parameters also indicate that expansion of the c axis is reversible (Table 4.1), which implies that Mg ions might have been reversibly inserted into TiSe_2 and located at the vacant van der Waals layers perpendicular to the c axis.

Table 4.1 Calculated structural parameters of Mg_xTiSe_2 from the diffraction patterns in Figure 4.18, using the same space group $P-3m1$.

Mg_xTiSe_2	$a / \text{\AA}$	$c / \text{\AA}$
Initial (TiSe_2)	3.5393(2)	6.0103(3)
Discharged	3.5691(8)	6.1076(8)
Charged	3.542(2)	6.027(4)

In order to reveal the structural changes during such a possible Mg insertion process based on the laboratory results, one discharged sample after 10 cycles has been studied by synchrotron X-ray diffraction at KEK-PF (BL-4B2) under the user project No. 2011G683. Rietveld analysis was applied to the diffraction patterns of TiSe_2 and Mg_xTiSe_2 (Figure 4.19). A structural model from the ICDD database (PDF#30-1383) was used in the analysis.

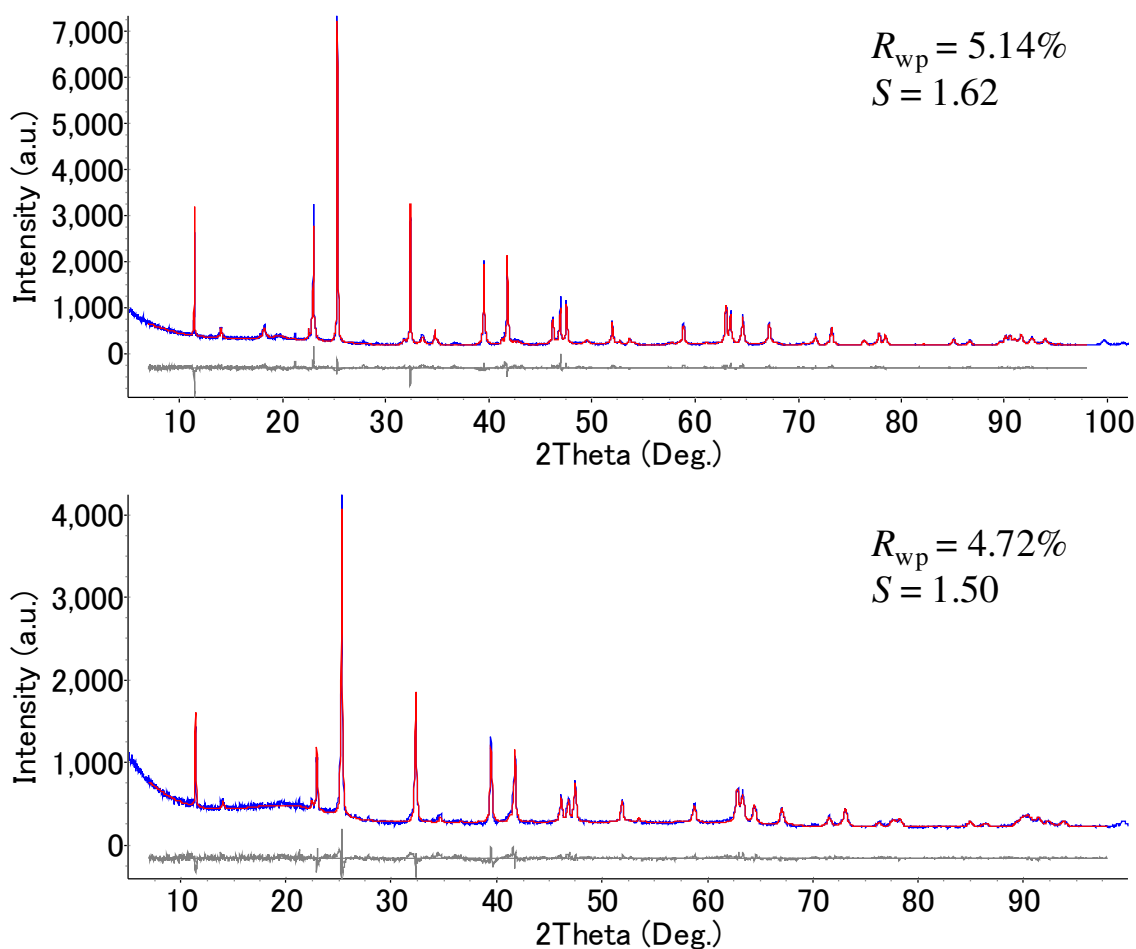


Figure 4.19 Synchrotron X-ray diffraction patterns of TiSe_2 (upper) and Mg_xTiSe_2 (lower). Both samples were sealed in capillary tubes. Fitting profiles and obtained parameters by Rietveld analysis are shown in each figure.

Difference Fourier analysis was performed between the structural model (TiSe_2) and the discharged electrode (Mg_xTiSe_2). The difference Fourier map shows that the electron density mainly distributes between the $[\text{TiSe}_2]$ slabs, which indicates that Mg ions might be inserted into the vacant van der Waals layers. But at present we could not identify the position or coordination of these Mg sites from the difference Fourier map, which might be due to the very small amount of Mg ions inserted into the Mg_xTiSe_2 sample.

Both octahedral and tetrahedral vacant sites exist in the van der Waals layers. In Li_xTiS_2 , Li ions are reported to be located at the octahedral sites.[60] By assuming that Mg ions might be inserted into the octahedral sites like Li ions considering they have similar ionic radii, Mg occupancy is calculated to be $x = 0.09(1)$ in Mg_xTiSe_2 . The refined structural parameters indicate a very small expansion of a and c axes (Table 4.2), if

compared to the laboratory results (Table 4.1).

Table 4.2 Refined structural parameters of TiSe_2 and Mg_xTiSe_2 , from the diffraction patterns in Figure 4.19.

TiSe_2 : space group $P-3m1$, $a = 3.53983(3) \text{ \AA}$, $c = 6.01106(6) \text{ \AA}$

Atom site	x	y	z	occupancy
Ti1	0	0	0	1
Se1	1/3	2/3	0.2567(1)	1

Mg_xTiSe_2 : space group $P-3m1$, $a = 3.5433(1) \text{ \AA}$, $c = 6.0240(2) \text{ \AA}$

Atom site	x	y	z	occupancy
Ti1	0	0	0	1
Se1	1/3	2/3	0.2547(4)	1
Mg1	0	0	0.5	0.09(1)

Such a small structural expansion in the discharged sample might be caused during the sample preparation. Capillary tubes made of Lindemann glass are used in the synchrotron X-ray diffraction since they are of negligible X-ray absorption. But the electrode samples have to be filled in the air, because these glass tubes are extremely fragile and it is too difficult to manipulate them in a glovebox. Our study have confirmed that exposure to air would cause the structure of Mg_xTiSe_2 to change back to the initial TiSe_2 phase (Figure 4.20), resulting in a small expansion of a and c axes. The same phenomenon is also reported in $\text{Mg}_x\text{Mo}_6\text{S}_8$.^[61]

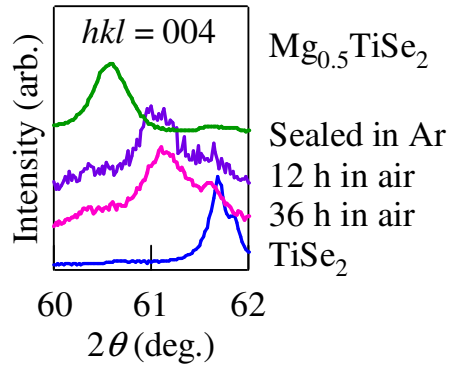


Figure 4.20 Comparison of the 004 reflection in $\text{Mg}_{0.5}\text{TiSe}_2$ (under various conditions) and TiSe_2 by X-ray diffraction.

Chemical analysis of the same electrode sample (in synchrotron X-ray diffraction) by ICP-AES shows that the composition of inserted Mg ions is $x = 0.249$, which is consistent with the result from our electrochemical measurement ($x = 0.24$). The less inserted Mg content than the electrochemical cycling test (than the values in Figure 4.15) might be due to incomplete Mg^{2+} diffusion in the large amount of electrode materials used in the cell for synchrotron X-ray diffraction. For further investigation of the Mg inserted structure, capillary samples prepared in a glovebox using less fragile glass materials (*like quartz glass, but it has a background in X-ray diffraction.*) are preferred.

4.4.3 Enhanced electrode performance in TiSe_2 by itinerant $4p$ orbitals - Comparison between Mg_xTiS_2 and Mg_xTiSe_2

TiS_2 , the best known transition metal disulfide as an insertion material for rechargeable lithium batteries,[60] has been tested as a magnesium battery cathode for the comparative study with Mg_xTiSe_2 . TiS_2 has the same layered structure as TiSe_2 (Figure 4.11) with hybridized Ti $3d$ and S $3p$ from the calculated orbital energy levels (Figure 4.10), which is also considered as a potential candidate material. Electrochemical charge and discharge curves of Mg/TiS_2 cells display a specific capacity *ca.* 20 mAh/g on cycling (Figure 4.21), which is much lower than Mg_xTiSe_2 (Figure 4.15).

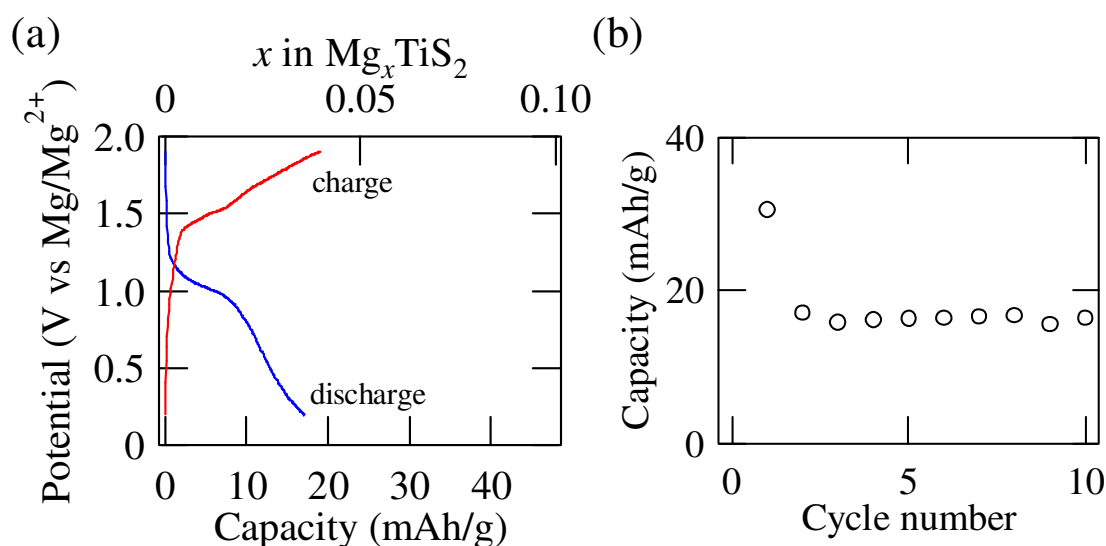


Figure 4.21 (a) Charge-discharge curves of Mg_xTiS_2 (the second cycle). (b) Capacity retention of Mg_xTiS_2 . The cell has been continuously cycled at 5 mA/g.

A general consideration would be that Mg_xTiS_2 should have shown a higher specific capacity since the molecular weight of TiS_2 is smaller than that of TiSe_2 (S: 32.07 g/mol; Se: 78.96 g/mol). But the experimental results indicate that despite of the same crystal structure, more Mg ions could be inserted into TiSe_2 rather than TiS_2 (Figure 4.22), which is obviously contradictory to the common experience.

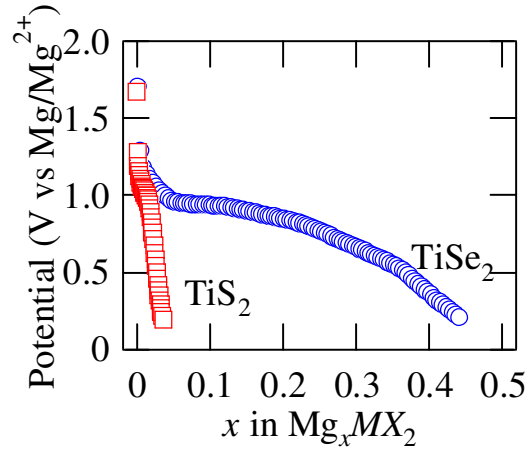


Figure 4.22 Mg insertion compositions (x) in Mg_xTiS_2 and Mg_xTiSe_2 , calculated from discharge capacities in Figure 4.15 and Figure 4.21.

In order to clarify the reason for their different performance, the particle size of active materials was firstly investigated by SEM, because a small particle size can effectively improve the electrode performance, which might have happened in the $\text{TiS}_2/\text{TiSe}_2$ case. Surprisingly, TiS_2 showed a smaller particle size (*ca.* 1 μm) than TiSe_2 (*ca.* 10 μm) (Figure 4.23), which is also contradictory to our expectations.

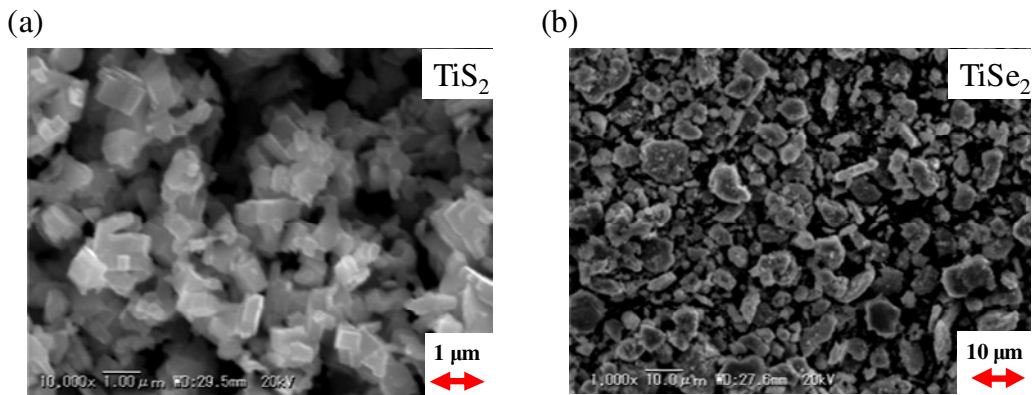


Figure 4.23 SEM images of (a) TiS_2 and (b) TiSe_2 . The average particle size is 1 μm and 10 μm respectively.

The electronic structure of the two compounds was then studied. Although both TiS_2 and TiSe_2 have hybridized d and p orbitals, the extent of p wave functions might be different because Se $4p$ can extend further than S $3p$ thus hybridizes more with Ti $3d$. The d - p hybridization can be roughly estimated by calculating the overlap integral of d and p orbitals (results are given in Section 4.6.2). Such a difference in the electronic structure finally results in the different electrode performance between $3p$ and $4p$ ligand systems. Increased capacity of the d - p hybridized selenide system is also reported in Mo_6S_8 .^[62]

This trend has been observed in a systematic examination of the electrode performance of transition metal chalcogenides (MX_2 and MX_3 ; M = transition metals from Group IVB to Group VIB; X = S, Se). Experimental results will be discussed in Section 4.6.2.

4.5 Magnesium battery cathode material: TiS_3

TiS_3 has a one-dimensional structure with infinite chains of $[\text{TiS}_6]$ prisms along the b axis (Figure 4.24 (a)). Van der Waals layers are perpendicular to the c axis (Figure 4.24 (b)). TiS_3 might exhibit a large capacity since TiS_3 is reported to have a discharge capacity over *ca.* 300 mAh/g as a lithium battery electrode (Figure 4.25). [63]

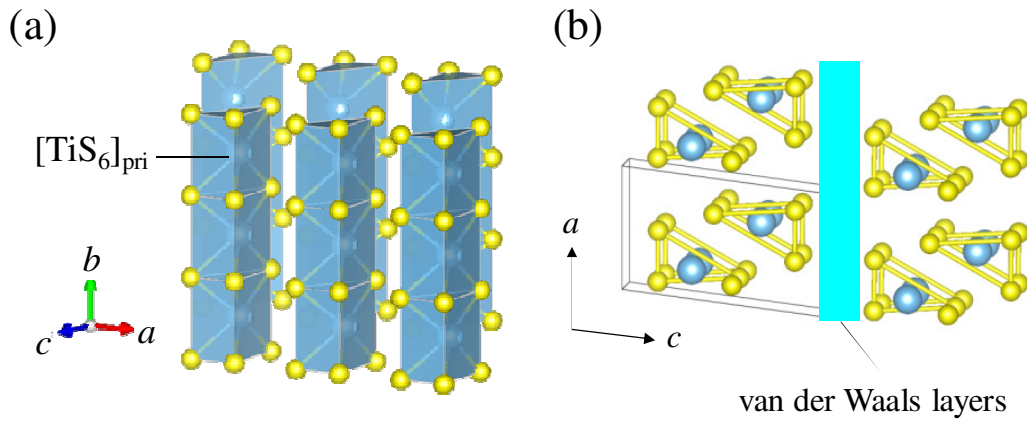


Figure 4.24 (a) The crystal structure of TiS_3 , consisting of $[\text{TiS}_6]$ prisms forming chains along the b direction. (b) View of van der Waals layers in the ac plane.

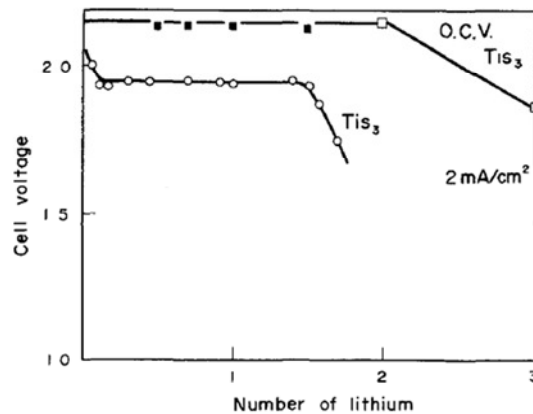


Figure 4.25 Discharge curves of Li/TiS_3 (electrolyte: LiClO_4 in dioxolane). The calculated specific capacity for Li_xTiS_3 is $186x$ mAh/g. [63]

The band calculation shows that TiS_3 is a narrow-gap semiconductor (Figure 4.26), which is also considered suitable for electrode applications since conductivity might be enhanced during the insertion process. Calculated DOS shows hybridized d and p

orbitals near the Fermi energy level (Figure 4.27).

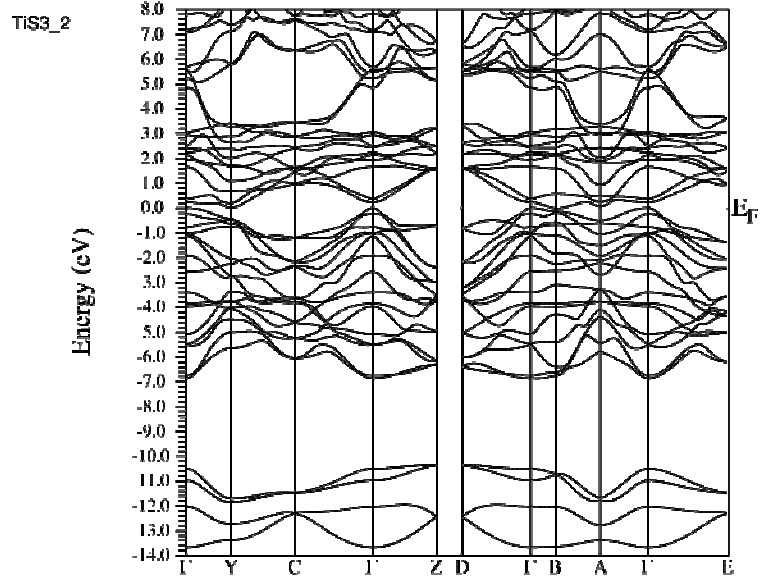


Figure 4.26 The band structure of TiS_3 .

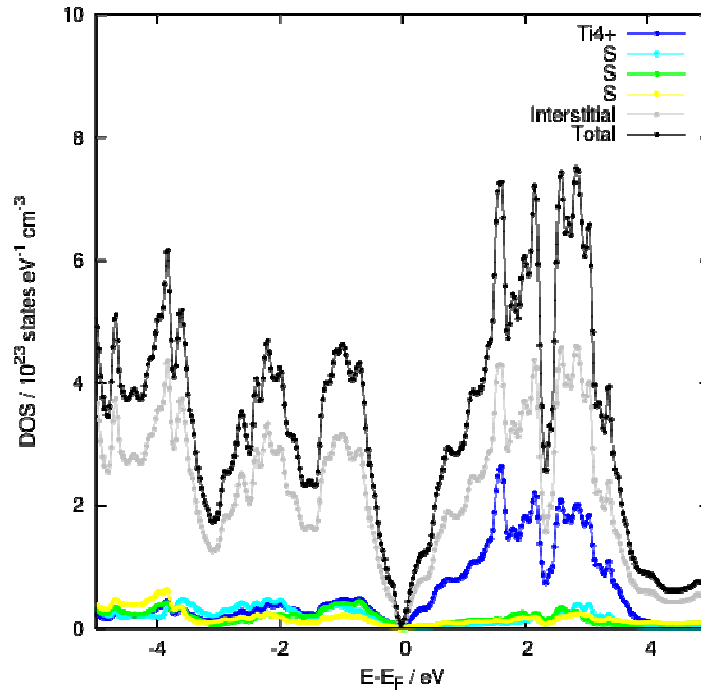


Figure 4.27 Calculated DOS of TiS_3 .

4.5.1 Material synthesis

TiS₃ was synthesized from titanium and sulfur by solid state reaction. The raw materials were mixed and heated at 500 °C for 72 hours in a sealed quartz tube. X-ray diffraction results show that TiS₃ has a $P2_1/m$ space group (Figure 4.28). Because the synthesized sample appears to be highly orientated along the c axis (almost only strong 00 l diffraction peaks were observed in the X-ray diffraction pattern), its structural parameters could not be obtained under present laboratory conditions.

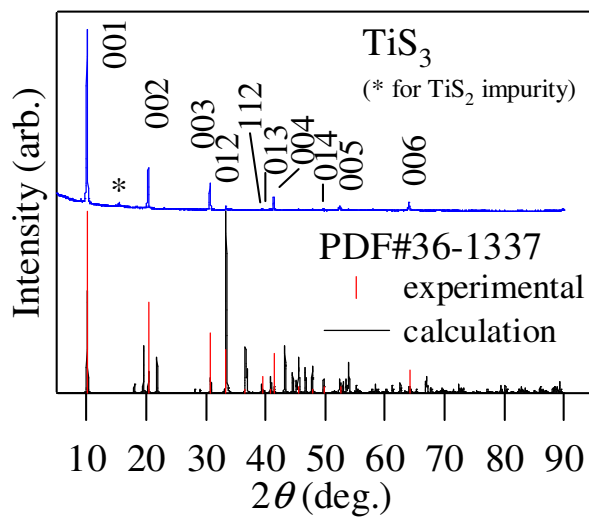


Figure 4.28 X-ray diffraction patterns of the TiS₃ sample and reference data.

SEM study confirmed that synthesized TiS₃ crystals were needle-shaped, with an average width size of *ca.* 10 μm (Figure 4.29).



Figure 4.29 The SEM image of TiS₃. The average width is around *ca.* 10 μm.

4.5.2 Reversible charge-discharge reactions in Mg/TiS₃

Despite the existence of needle-shaped crystals even after the grinding process, electrochemical tests of Mg/TiS₃ cells achieved a specific capacity of *ca.* 80 mAh/g (Figure 4.30 (a)), comparable to the reported Mg/Mo₆S₈ system (*ca.* 75 mAh/g). The potential curve slopes from about 1 V (vs Mg/Mg²⁺) down to the cut-off voltage. Charge-discharge cycling was repeated reversibly over 50 cycles, with the capacity gradually fading to *ca.* 80 mAh/g (Figure 4.30 (b)).

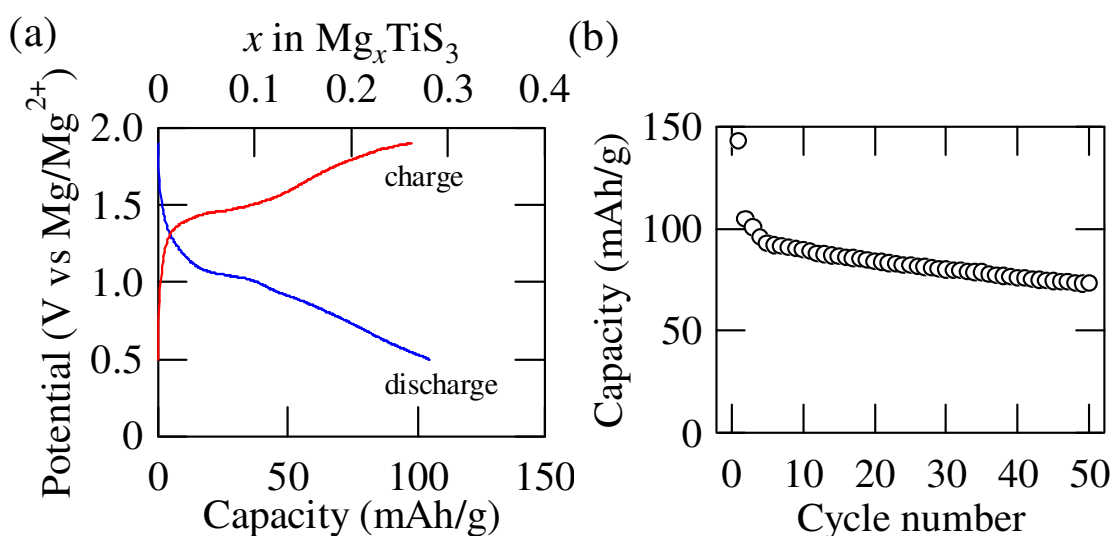


Figure 4.30 (a) Charge-discharge curves of Mg_xTiS₃ (the second cycle). (b) Capacity retention of Mg_xTiS₃. The cell has been continuously cycled.

Preliminary *Ex situ* structural analysis shows that the TiS₃ structure is kept in Mg_xTiS₃ (Figure 4.31), so that there is no conversion reaction on discharge. However, due to the highly orientated TiS₃ structure, no other structural information could be obtained from the structural study under present experimental conditions. Further investigation is needed to reveal possible structural changes during charge-discharge reactions.

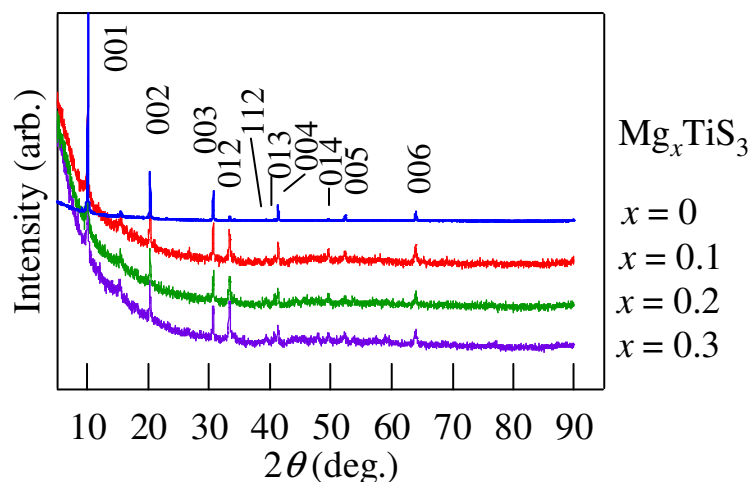


Figure 4.31 X-ray diffraction patterns of Mg_xTiS_3 electrodes with different x values.

4.5.3 The possibility of high storage capacity - Rate capability of Mg_xTiS_3

Mg/TiS_3 cells have been tested at various discharge rates (Figure 4.32). The discharge capacity decreases to almost zero at a high current density of 50 mA/g, which is very different from the high rate behavior of Mg/TiSe_2 (Figure 4.16). The difference between Mg_xTiS_3 and Mg_xTiSe_2 might be explained by relatively low intrinsic electrical conductivity of TiS_3 (semiconducting) compared to TiSe_2 (metallic). In addition to the particle size and morphology of TiS_3 (needle shaped microcrystals), electrical conductivity might be the barrier under high rate cycling and limits its rate capability.

Since the discharge capacity decreases rapidly at high current rates, Mg_xTiS_3 was tested again at a very slow rate (0.001 C, the theoretical capacity is assumed to be $\text{Mg}_{1.5}\text{TiS}_3$ or Li_3TiS_3 , from OCV in Figure 4.25) to investigate the possibility of large capacity like in Li_xTiS_3 . As a result, a specific capacity of ca. 300 mAh/g (Figure 4.33) was obtained, which is comparable to Li_xTiS_3 (Figure 4.25). Further optimizations should at least include the enhancement of electronic conductivity and downsizing particle sizes so as to improve the electrode performance.

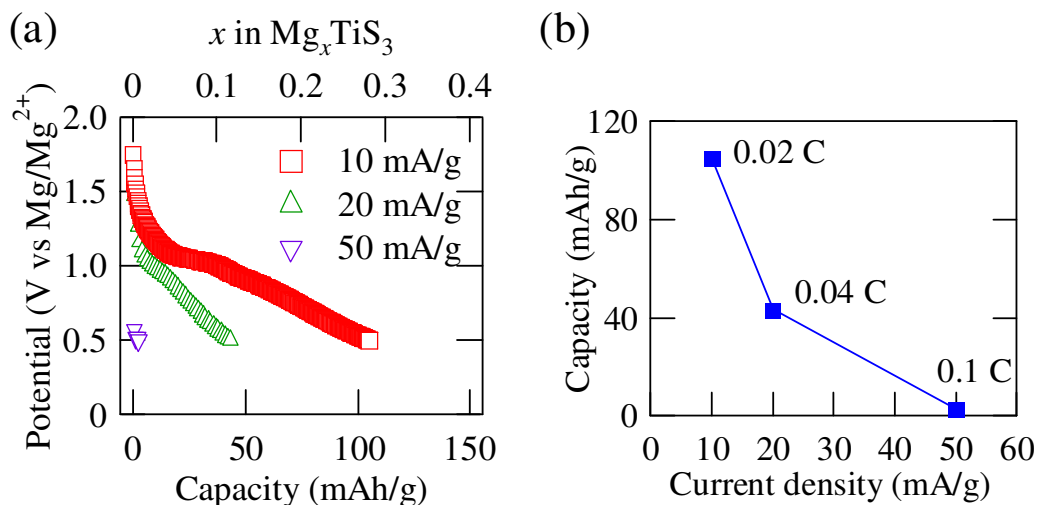


Figure 4.32 (a) Discharge curves and (b) capacity retention of Mg_xTiS_3 at different current densities. The C rate is based on a theoretical specific capacity of 558 mAh/g ($\text{Mg}_{1.5}\text{TiS}_3$).

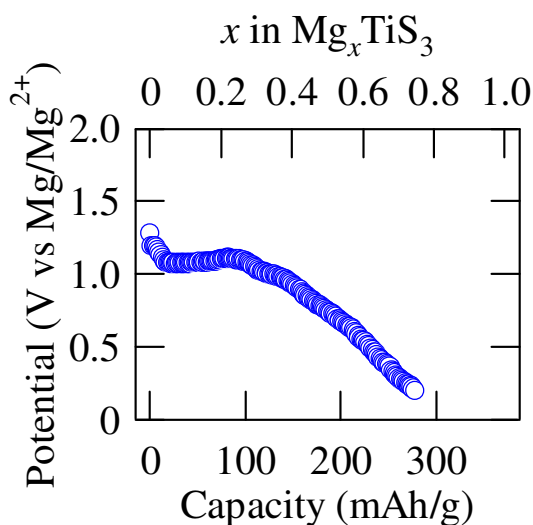


Figure 4.33 The discharge curve of Mg_xTiS_3 at a 0.001 C rate (0.5 mA/g).

We have also tried to compare the electrochemical behavior between Mg_xTiS_3 and Mg_xTiSe_3 (like the comparison between Mg_xTiS_2 and Mg_xTiSe_2 in Section 4.4.3). But the successful synthesis of TiSe_3 has never been reported, and we also failed in the synthesis of TiSe_3 in this study. Electrochemical results in other trichalcogenides (MX_3 in Table 4.4) confirmed that the effect of itinerant Se 4p orbitals could enhance electrode performance of trichalcogenides, which is consistent with the results in dichalcogenides (Section 4.4.3 and MX_2 in Table 4.4).

4.6 Roles of *d-p* hybridization in magnesium battery electrodes

4.6.1 Larger capacities are observed in *d-p* hybridized systems

In order to clarify whether the hybridized *d* and *p* orbitals have been linked to the electrode performance in our materials TiSe₂ and TiS₃, a weakly *d-p* hybridized material TiO₂ as well as other selected compounds (V and Mo related oxides and chalcogenides) have been tested as magnesium battery electrodes. Although the three oxides (TiO₂, V₂O₅, MoO₃) are well-known lithium battery materials that can reversibly host Li ions, they all show very small insertion levels in magnesium batteries (See Figure 5.2 (a-f) in Supplementary Information).

Generally Li ions can insert into almost every host materials having void spaces, thus their different behaviors in magnesium batteries might be related to electronic structures (See the summarized data in Table 4.3).

Table 4.3 Measured typical discharge capacities of selected compounds as magnesium battery cathodes, with the energy difference between transition metal *d* and ligand anion *p* orbitals ($|E_d - E_p|$).

Transition metal	Compound	$ E_d - E_p /\text{eV}$	Capacity (mAh/g)
Ti	TiO ₂	5.68	3 (Figure 5.2 (a))
	TiS ₂	0.56	20 (Figure 4.21 (a))
	TiSe ₂	0.36	110 (Figure 4.15 (a))
	TiS ₃	0.56	80 (Figure 4.30 (a))
V	V ₂ O ₅	4.17	7 (Figure 5.2 (b))
	VSe ₂	1.87	100 (Figure 5.2 (d), [66])
Mo	MoO ₃	5.16	4 (Figure 5.2 (c), [66])
	MoS ₂	0.04	5 (Figure 5.2 (e), [66])
	MoSe ₂	0.88	20 (Figure 5.2 (f), [66])
	Mo ₆ S ₈	0.04	75 (from [36])

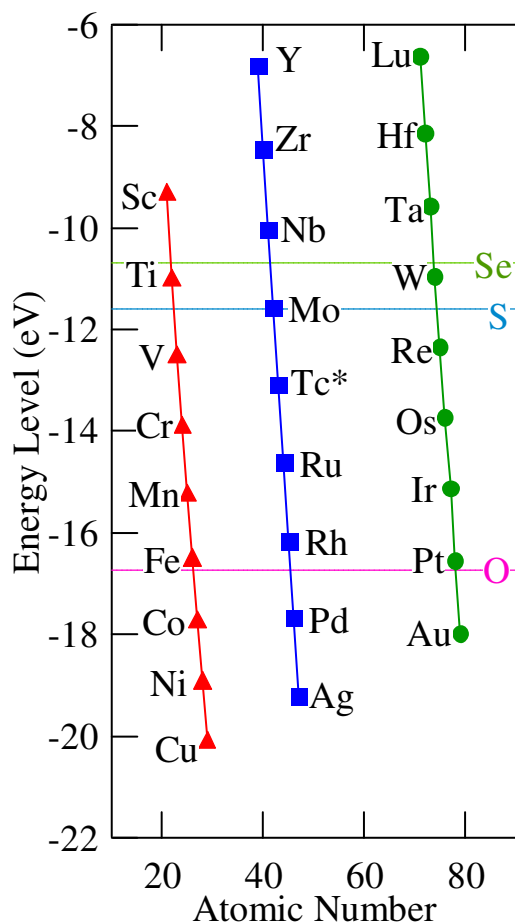


Figure 4.34 Orbital energy levels for transition metals (3*d*, 4*d* and 5*d* orbitals) and oxygen 2*p*, sulfur 3*p*, selenium 4*p* orbitals. [57][58]

The energy difference between *d* and *p* orbitals ($|E_d - E_p|$ in Table 4.3, calculated from Figure 4.34) are used to estimate how much they hybridize with each other in these compounds. Ti, V and Mo are early transition metals and their *d* orbital levels are near *p* levels of S or Se, while their oxides have a large energy difference (> 4 eV) due to weakly hybridized *d* and *p* orbitals. Therefore it is not surprising that Mg ions could hardly be inserted into TiO_2 , V_2O_5 and MoO_3 as reported by other research groups (Section 4.2.3), compared to large capacities in strongly hybridized sulfide and selenide systems (except for MoS_2 , which will be discussed in Section 4.6.3).

4.6.2 Itinerant 4*p* orbitals effectively hybridize with *d* orbitals and display superior electrode performance to 3*p* systems

An interesting phenomenon which could be observed in the previous section (Table 4.3) is that selenides tend to show larger capacities than their analogous sulfides (TiX₂, VX₂ and MoX₂, X = S or Se), despite the fact that in both selenides and sulfides *d-p* hybridization is expected to exist according to orbital energy levels (Figure 4.34). This phenomenon has been further investigated on layered dichalcogenides (MX₂) and trichalcogenides (MX₃) by measuring their performance as magnesium battery cathodes. Experimental results show that selenides could host more Mg ions than sulfides (See Figure 5.3 in Supplementary Information).

Therefore, benefiting from the larger Mg insertion compositions, selenides have displayed higher discharge capacities than sulfides in magnesium batteries (Table 4.4) (except for TaX₂, which will be discussed in Section 4.6.3). However, the particle size is not a crucial factor here affecting electrode performance, because selenides even show larger particle sizes than sulfides (TiS₂ ~ 1 μm, TiSe₂ ~ 10 μm; ZrS₂ ~ 20 μm, ZrSe₂ ~ 50 μm; MoS₂ ~ 1 μm, [66] MoSe₂ ~ 100 μm, [66] etc.). It is difficult to understand such a phenomenon if only considering that they share the same layered crystal structure and selenides have heavier molecular weights.

Table 4.4 Summary of measured typical specific capacities (in mAh/g) of MX₂ and MX₃ (M = transition metals; X = S, Se) as magnesium battery cathodes. (Numbers in parentheses are discharge capacities in the first cycle. Results of some compounds that have not been tested are left blank "-".)

M	MS ₂	MSe ₂	MS ₃	MSe ₃
Ti	20(30)	110(130)	80(140)	-
V	-	100(125)	-	-
Cr	-	-	-	-
Zr	5(10)	75(70)	10(28)	20(42)
Nb	2(5)	18(10)	22(53)	25(62)
Mo	5(10)	20(28)	-	-
Hf	8(10)	26(35)	-	-
Ta	23(26)	5(11)	-	-
W	6(8)	7(11)	-	-

We here propose that the itinerant character of Se 4*p* orbitals might have played an important role in the different capacity performance. Although these early transition metal chalcogenides have hybridized *d* and *p* orbitals, the extent of *p* wave functions should be different because Se 4*p* can extend further than S 3*p* and thus hybridizes more with *d* orbitals.

The extent difference between 3*p* and 4*p* can be roughly estimated by calculating the radical part of the overlap integral of M *d* and X *p* orbitals: $\left| \int_0^{\infty} R_p(X)R_d(M)r^2dr \right|$. In the

layered dichalcogenides (Table 4.5), itinerant Se 4*p* orbitals show several orders of magnitude larger integral values ($\sim 10^{21}$) than S 3*p* ($\sim 10^{12}$), which indicates that selenides are much more hybridized systems and thus could assist the insertion process of bivalent Mg ions more effectively. Because selenides have heavier molecular weights than sulfides, their larger or even comparable specific capacities proved that more Mg ions could be reversibly hosted.

Table 4.5 Calculated integral values of $|\int R_p R_d r^2 dr|$ for layered MX₂ compounds (M = transition metals; X = S, Se).

M	MS ₂	MSe ₂
Ti	9.06×10^{12}	5.77×10^{21}
V	3.99×10^{12}	2.25×10^{21}
Cr	6.06×10^{12}	1.24×10^{21}
Zr	5.90×10^{12}	14.5×10^{21}
Nb	1.51×10^{12}	5.39×10^{21}
Mo	0.755×10^{12}	0.696×10^{21}
Hf	12.3×10^{12}	6.32×10^{21}
Ta	2.97×10^{12}	1.05×10^{21}
W	2.43×10^{12}	0.726×10^{21}

The effect of itinerant Se 4*p* orbitals is also proved in other systems. In trichalcogenides MX₃ (Table 4.4), although the capacity difference is not as remarkable as in the dichalcogenides, selenides still display larger capacities than sulfides. Increased capacity is also reported in Mo₆X₈,[62] in which the specific capacity was improved by substituting 1 or 2 sulfur atoms with selenium.

4.6.3 Further discussions on the effect of M-X coordination in MX₂

Results of layered dichalcogenides could be further divided into two groups based on the M-X coordination geometry. Usually two types of coordination exist in the layered dichalcogenides, octahedral and trigonal prismatic (Figure 4.35), and which type a compound takes mainly depends on the number of *d* electrons.

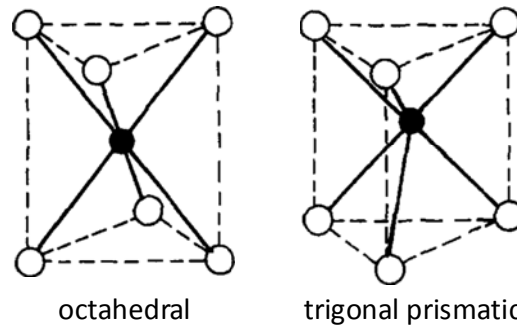


Figure 4.35 Schematic illustrations of different M-X coordination geometries in layered dichalcogenides.

It appears that layered dichalcogenides with octahedral M-X coordination display larger capacities of Mg ions than those of trigonal prismatic M-X coordination (Figure 4.36). Although both types of coordination have quite similar crystal structures, their electronic properties especially the band structure might vary due to different symmetries in the crystal field splitting related to different electron configurations.

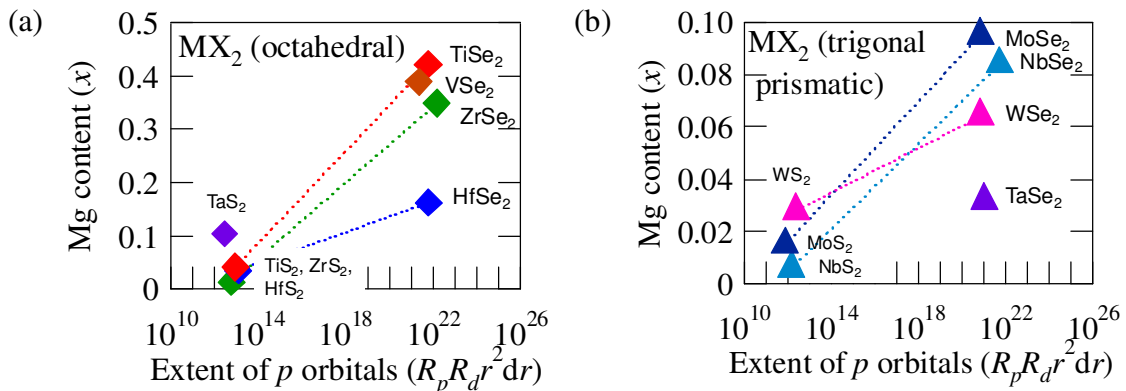


Figure 4.36 Mg insertion compositions versus integral values of $|\int R_p R_d r^2 dr|$ for MX₂ compounds with different M-X coordination geometries: (a) octahedral, (b) trigonal prismatic.

Group VI chalcogenides (d^2 configuration MoX_2 and WX_2) all adapt trigonal prismatic coordination to depress the filled d_{z^2} band in the splitting (Figure 4.37). The trigonal prismatic splitting creates a small band gap between the lower filled d_{z^2} and other upper empty d bands, which is confirmed by our band calculations that a band gap (~ 1 eV) exists in all Group VI chalcogenides. Thus it is not easy for electrons entering the system with a relatively wide band gap (Figure 4.36 (b)) compared to the narrow gaps in Group IV (See below). Besides, a d^3 configuration in the trigonal prismatic coordination would cause the system becoming thermodynamically unstable. (For example, the Li/MoS_2 system was abandoned at first due to its poor electrode performance, until later people found that if the system is forced to discharge at a very low potential upon Li intercalation MoS_2 will transform from trigonal prismatic to octahedral coordination and reversible performance in octahedral coordination has met practical applications.[64])

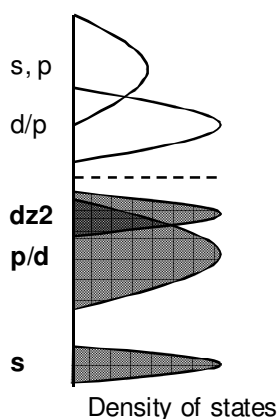


Figure 4.37 Schematic illustrations of the density of states for trigonal prismatic M-X coordination compounds: MoX_2 and WX_2 (d^2 configuration). A band gap (1 eV) is created in all d^2 MX_2 compounds.

Group IV chalcogenides (d^0 configuration TiX_2 , ZrX_2 , HfX_2) as well as VSe_2 (d^1) favor octahedral coordination in which chalcogen anions do not need to face each other. Band calculations show that ZrS_2 has a band gap (~ 1 eV) between filled p and empty d_{z^2} bands while other compounds are either metallic or having narrow gaps (< 0.3 eV) (Figure 4.38). Experimental results also indicate that these d^0 or d^1 chalcogenides in octahedral coordination have better electrode performance than chalcogenides in trigonal prismatic coordination (Figure 4.36 (a)).

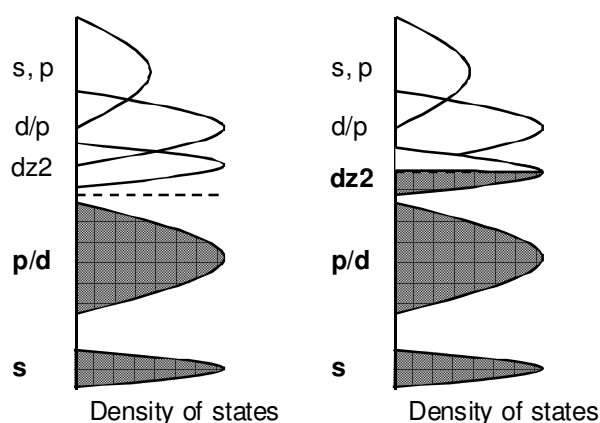


Figure 4.38 Schematic illustrations of the density of states for octahedral M-X coordination compounds: TiX_2 , ZrX_2 , HfX_2 (d^0 , left) and VSe_2 (d^1 , right).

The rest Group V chalcogenides (d^1 configuration NbX_2 and TaX_2) with a half filled d_{z2} band can crystallize in both types of M-X coordination (Figure 4.39). In TaX_2 its sulfide exhibits a larger capacity than selenide which might be attributed to their difference coordination symmetries (Table 4.4). Results of this group are consistent with the entire experimental picture that materials with octahedral coordination have higher storage capacities than those with trigonal prismatic coordination. But their electrode behaviors needs to be further investigated and explained due to the complicated electronic properties.

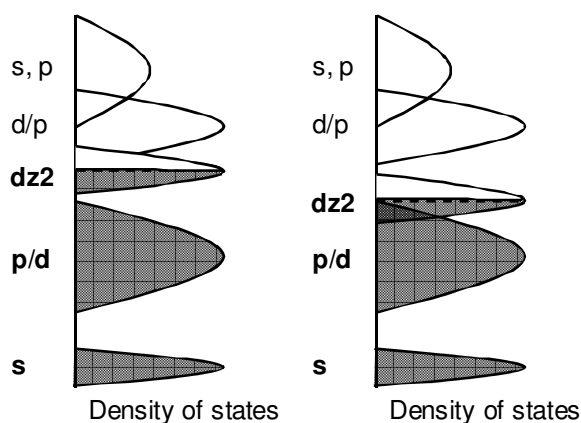


Figure 4.39 Schematic illustrations of the density of states for the compounds that adapt both types of M-X coordination: octahedral (left) and trigonal prismatic (right). The examples of compounds are NbX_2 and TaX_2 (d^1).

4.7 Perspectives for future research on magnesium batteries

In summary, reversible charge-discharge reactions are obtained in TiSe_2 and TiS_3 , compounds of totally different crystal structures as candidate materials for magnesium batteries. Both materials show higher or comparable specific capacities compared the representative $\text{Mg/Mo}_6\text{S}_8$ system. Their reversible electrode performance might be attributed to hybridized d and p orbitals which could moderate charge redistribution caused by bivalent Mg ions in the local structure. We propose hybridized d - p systems would be a clear guideline for exploring electrode materials of magnesium batteries and even other multivalent-ion batteries (Al^{3+} , Ca^{2+} , etc.) that depend strongly on the electronic structure of electrodes.

This work has focused on d - p hybridized sulfides and selenides of early transition metals due to the electrochemical window limit in the electrolyte, since electrode materials with early transition metals have relatively low operating potentials. An immediate extent of our study would be oxide materials using late transition metals (Figure 4.34), which must require a new electrolyte system with a wider potential window. However, the low intrinsic electrical conductivity of oxides might be problematic in a practical electrode process, where optimizations including nanosized materials or carbon coating processes are needed.[65]

If we can utilize all possible elements across the periodic table to design electrode materials, the "element strategy" for low cost materials could be realized in future material research. For example, since the number of oxides and chalcogenides is still limited, we could develop materials with other anions to form a d - p hybridized system (F, Cl, P, etc.). Besides, we might also use the combination of transition metal elements or anions of different orbital energy levels to adjust the band structure and "create" potential candidate materials.

Chapter 5: Supplementary Information

5 Supplementary Information

5.1 The equilibrium potential in a two-phase reaction

The equilibrium characteristic in a two-phase reaction can be well interpreted based on thermodynamic theories. In the composition range $x_1 < x < x_2$, the system's Gibbs energy $G(x)$ following the common tangent line of the two phases is lower than each phase's Gibbs energy curve (Figure 5.1). Thus the system tends to gain more energy by separating into two phases rather than forming a solid solution to follow either single phase's Gibbs energy curve. The system's Gibbs energy is independent of the composition (a) at the point x :

$$G(x) = a G_2(x_2) + (1-a) G_1(x_1) = \frac{G_2(x_2) - G_1(x_1)}{x_2 - x_1} \cdot x + \frac{x_2 G_2(x_2) - x_1 G_1(x_1)}{x_2 - x_1}$$

The cell voltage (E), which can be expressed as the differential of the system's Gibbs energy, has then to be a constant value since the variation of Gibbs energy with composition is a straight line within $x_1 < x < x_2$.

$$E = -\frac{1}{F} \cdot \frac{dG}{dx} = -\frac{1}{F} \cdot \frac{G(x_2) - G(x_1)}{x_2 - x_1} = \text{const.}$$

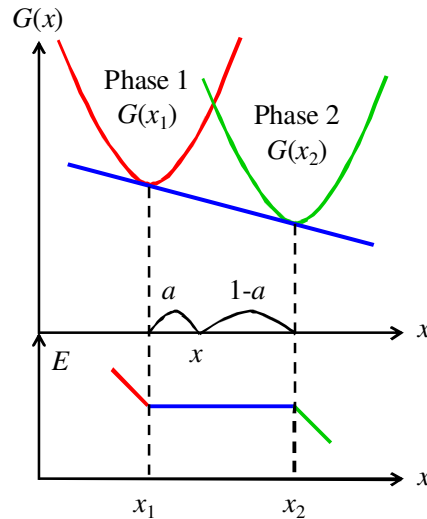


Figure 5.1 Variation of Gibbs energy (G) and voltage (E) with composition (x) in the two-phase region ($x_1 < x < x_2$; at Point x the system separates into Phase 1 and Phase 2, with composition values of a and $(1-a)$ respectively.)

5.2 Additional results of materials as magnesium battery cathodes

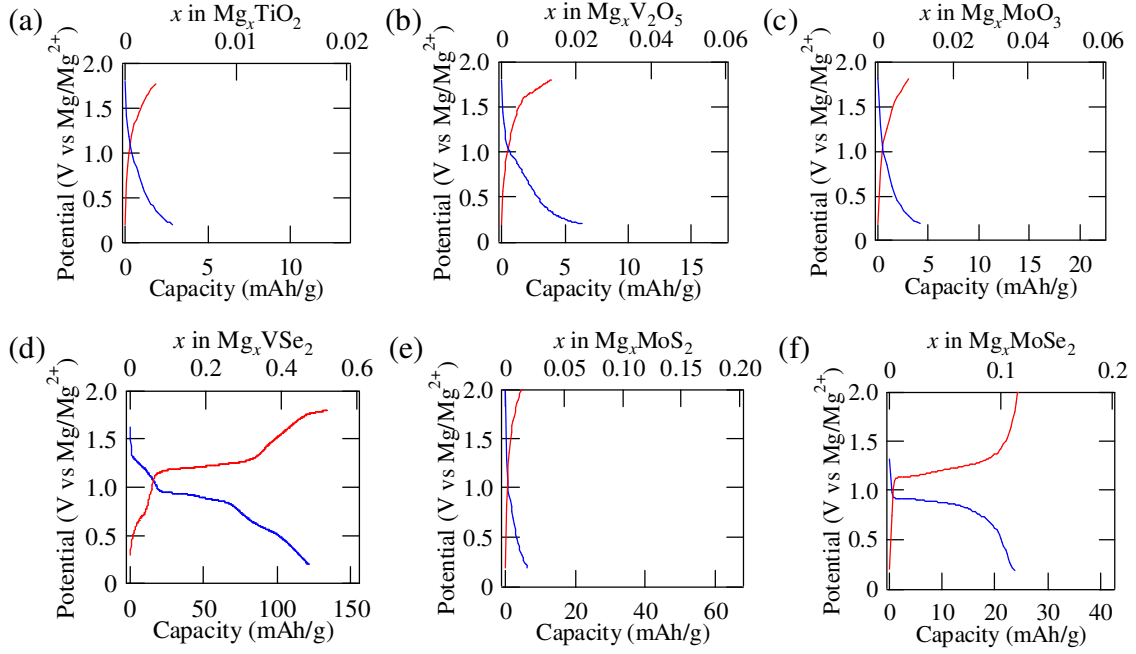


Figure 5.2 Typical charge and discharge curves of (a) TiO_2 , (b) V_2O_5 , (c) MoO_3 , [66] (d) VSe_2 , [66] (e) MoS_2 , [66] and (f) MoSe_2 . [66] (Data of MoS_2 and MoSe_2 are drawn to the same scale for comparing the amount of inserted Mg ions.)

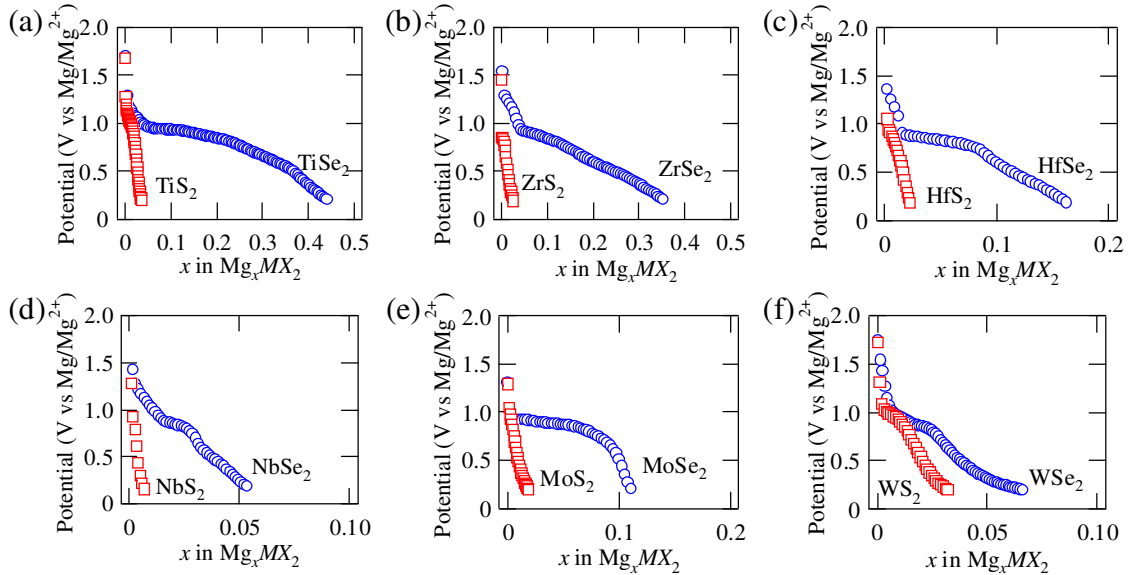


Figure 5.3 Comparison of Mg insertion compositions between sulfide/selenide pairs of layered dichalcogenides: (a) TiS_2 and TiSe_2 , (b) ZrS_2 and ZrSe_2 , (c) HfS_2 and HfSe_2 , [66] (d) NbS_2 and NbSe_2 , (e) MoS_2 and MoSe_2 , [66] (f) WS_2 and WSe_2 .

Chapter 6: References

6 References

- [1] M. Armand, J. -M. Tarascon, *Nature*, 2008, 451, 652.
Building better batteries (Review)
- [2] M. Winter, J. O. Besenhard, M. E. Spahr, P. Novak, *Adv. Mater.*, 1998, 10, 725.
Insertion Electrode Materials for Rechargeable Lithium Batteries (Review)
- [3] M. Hibino, W. Han, T. Kudo, *Solid State Ionics*, 2000, 135, 61.
Electrochemical lithium intercalation into a hexagonal WO_3 frame work and its structural change.
- [4] 堀江英明. リチウムイオン電池 - 基礎と応用.
- [5] J. Reed, G. Ceder, *Chem. Rev.*, 2004, 104, 4513.
Role of Electronic Structure in the Susceptibility of Metastable Transition-Metal Oxide Structures to Transformation
- [6] F. Cheng, J. Liang, Z. Tao, J. Chen, *Adv. Mater.*, 2011, 23, 1695.
Functional Materials for Rechargeable Batteries (Review)
- [7] T. Ohzuku, A. Ueda, N. Yamamoto, *J. Electrochem. Soc.*, 1995, 142, 1431.
Zero-Strain Insertion Material of $\text{Li}[\text{Li}_{1/3}\text{Ti}_{5/3}]\text{O}_4$ for Rechargeable Lithium Cells
- [8] S. Scharner, W. Weppner, P. Schmid-Beurmann, *J. Electrochem. Soc.*, 1999, 146, 857.
Evidence of Two-Phase Formation upon Lithium Insertion into the $\text{Li}_{1.33}\text{Ti}_{1.67}\text{O}_4$ Spinel
- [9] T. Ohzuku, M. Kitagawa, T. Hirai, *J. Electrochem. Soc.*, 1990, 137, 769.
Electrochemistry of Manganese Dioxide in Lithium Nonaqueous Cell - 3 Reduction of Spinel-Related MnO_2
- [10] A. K. Padhi, K. S. Nanjundaswamy, J. B. Goodenough, *J. Electrochem. Soc.*, 1997, 144, 1188.
Phospho-olivines as Positive-Electrode Materials for Rechargeable Lithium Batteries
- [11] C. Delacourt, P. Poizot, J. -M. Tarascon, C. Masquelier, *Nat. Mater.*, 2005, 4, 254.
The existence of a temperature-driven solid solution in Li_xFePO_4
- [12] A. Yamada, H. Koizumi, S. Nishimura, N. Sonoyama, R. Kanno, M. Yonemura, T. Nakamura, Y. Kobayashi, *Nat. Mater.*, 2006, 5, 357.
Room-temperature miscibility gap in Li_xFePO_4
- [13] C. Delmas, M. Maccario, L. Croguennec, F. Le Cras, F. Weill, *Nat. Mater.*, 2008, 7,

665.

Lithium deintercalation in LiFePO_4 nanoparticles via a domino-cascade model

[14] A. Yamada, S. C. Chung, K. Hinokuma, J. Electrochemical. Soc., 2001, 148, A224

Optimized LiFePO_4 for Lithium Battery Cathodes

[15] W. Dreyer, J. Jamnik, C. Gohlke, R. Huth, J. Moškon, M. Gaberšček, Nat. Mater., 2010, 9, 448.

The thermodynamic origin of hysteresis in insertion batteries

[16] M. Wagemaker, W. J. H. Borghols, F. M. Mulder, J. Am. Chem. Soc., 2007, 129, 4323.

Large Impact of Particle Size on Insertion Reactions. A Case for Anatase Li_xTiO_2

[17] M. Wagemaker, E. R. H. van Eck, A. P. M. Kentgens, F. M. Mulder, J. Phys. Chem. B, 2009, 113, 224.

Li-Ion Diffusion in the Equilibrium Nanomorphology of Spinel $\text{Li}_{4+x}\text{Ti}_5\text{O}_{12}$

[18] M. Wagemaker, D. R. Simon, E. M. Kelder, J. Schoonman, C. Ringpfeil, U. Haake, D. Lützenkirchen-Hecht, R. Frahm, F. M. Mulder, Adv. Mater., 2006, 18, 3169.

A Kinetic Two-Phase and Equilibrium Solid Solution in Spinel $\text{Li}_{4+x}\text{Ti}_5\text{O}_{12}$

[19] G. C. Amatucci, F. Badway, A. Du Pasquier, T. Zheng, J. Electrochem. Soc., 2001, 148, A930.

An Asymmetric Hybrid Nonaqueous Energy Storage Cell

[20] H. G. Jung, M. W. Jang, J. Hassoun, Y.-K. Sun, B. Scrosati, Nat. Commun., 2011, 2, 516.

A high-rate long-life $\text{Li}_4\text{Ti}_5\text{O}_{12}/\text{Li}[\text{Ni}_{0.45}\text{Co}_{0.1}\text{Mn}_{1.45}]\text{O}_4$ lithium-ion battery

[21] L. Zhao, Y. -S. Hu, H. Li, Z. Wang, L. Chen, Adv. Mater., 2011, 23, 1385.

Porous $\text{Li}_4\text{Ti}_5\text{O}_{12}$ Coated with N-Doped Carbon from Ionic Liquids for Li-Ion Batteries

[22] X. Lu, L. Zhao, X. He, R. Xiao, L. Gu, Y. -S. Hu, H. Li, Z. Wang, X. Duan, L. Chen, J. Maier, Y. Ikuhara, Adv. Mater., 2012, 24, 3233.

Lithium Storage in $\text{Li}_4\text{Ti}_5\text{O}_{12}$ Spinel - The Full Static Picture from Electron Microscopy

[23] J. B. Goodenough, Prog. Solid State Chem., 1971, 5, 145.

Metallic oxides (Review)

[24] Y. Okamoto, S. Niitaka, M. Uchida, T. Waki, M. Takigawa, Y. Nakatsu, A. Sekiyama, S. Suga, R. Arita, H. Takagi, Phys. Rev. Lett., 2008, 101, 086404.

Band Jahn-Teller Instability and Formation of Valence Bond Solid in a Mixed-Valent Spinel Oxide LiRh_2O_4

[25] A. Yamada, M. Tanaka, Mater. Res. Bull., 1995, 30, 715.

Jahn-Teller Structural Phase Transition Around 280K in LiMn_2O_4

- [26] A. Yamada, J. Solid State Chem., 1996, 122, 160.
Lattice Instability in $\text{Li}(\text{Li}_x\text{Mn}_{2-x})\text{O}_4$
- [27] G. Kobayashi, S. Nishimura, M.-S. Park, R. Kanno, M. Yashima, T. Ida, A. Yamada, Adv. Funct. Mater., 2009, 19, 395.
Isolation of Solid Solution Phases in Size-Controlled Li_xFePO_4 at Room Temperature
- [28] L. A. de Picciotto, M. M. Thackeray, Mat. Res. Bull., 1985, 20, 1409.
Insertion/extraction reactions of lithium with LiV_2O_4
- [29] M. Wagemaker, F. M. Mulder, A. Van der Ven, Adv. Mater. 2009, 21, 2703.
The Role of Surface and Interface Energy on Phase Stability of Nanosized Insertion Compounds
- [30] http://knowledge.allianz.com/mobility/alternative_fuels/?2068/Cheaper-batteries-will-charge-e-mobility
Cheaper batteries will charge e-mobility (Press release)
- [31] <http://www.greencarcongress.com/2010/11/leaf-20101122.html>
US EPA rates Nissan LEAF fuel economy as 99 mpg-equivalent (combined); 73-mile range (Press release)
- [32] <http://news.consumerreports.org/cars/2011/12/leaf-volt-tests-show-electric-cars-cost-less-per-mile-to-operate.html>
Leaf, Volt tests show electric cars cost less per mile to operate (Press release)
- [33] <http://www.bbc.co.uk/news/business-21054089>
Dreamliner: Boeing 787 planes grounded on safety fears (Press release)
- [34] http://www.nts.gov/investigations/2013/boeing_787/boeing_787.html
Boeing 787 Battery Fire (Press release)
- [35] <http://www.aviationwire.jp/archives/14821>
米運輸安全委、787 の APU 用バッテリー内部の写真公開 (Press release in Japanese)
- [36] D. Aurbach, Z. Lu, A. Schechter, Y. Gofer, H. Gizbar, R. Turgeman, Y. Cohen, M. Moshkovich, E. Levi, Nature, 2000, 407, 724.
Prototype systems for rechargeable magnesium batteries.
- [37] Clarke, F. W.; Washington, H. S. (1924). "The composition of the earth's crust". US. Geol. Surv. Prof. Paper: 127.
- [38] Z. Lu, A. Schechter, M. Moshkovich, D. Aurbach, J. Electroanalytical Chem., 1999, 466, 203.
On the electrochemical behavior of magnesium electrodes in polar aprotic

electrolyte solutions

- [39] A. Lisowska-Oleksiak, H. D. Inerowicz, J. Power Sources, 1999, 81-82, 813.
Study on poly(ethylene-oxide) electrolytes with ionophores for lithium batteries
- [40] D. Imamura, M. Miyayama, M. Hibino, T. Kudo, J. Electrochem. Soc. 2003, 150, A753.
Mg Intercalation Properties into V_2O_5 gel/Carbon Composites under High-Rate Condition
- [41] A. V. Murugan, B. B. Kale, C. W. Kwon, G. Camper, K. Vijayamohanan, J. Mater. Chem., 2001, 11, 2470.
Synthesis and characterization of a new organo-inorganic PEDOT/ V_2O_5 nanocomposite by intercalation
- [42] E. Levi, M. D. Levi, O. Chasid, D. Aurbach, J. Electroceram, 2009, 13, 13.
A review on the problems of the solid state ions diffusion in cathodes for rechargeable Mg batteries
- [43] E. Levi, Y. Gofer, D. Aurbach, Chem. Mater., 2010, 22, 860.
On the Way to Rechargeable Mg Batteries: The Challenge of New Cathode Materials (Review)
- [44] D. Aurbach, Y. Gofer, A. Schechter, Z. Lu, C. Gizbar, United States Patent, 2001, US 6316141 B1.
High-energy rechargeable electrochemical cells with non-aqueous electrolytes
- [45] D. Aurbach, H. Gizbar, A. Schechter, O. Chusid, H. E. Gottlieb, Y. Gofer, I. Goldberg, J. Electrochem. Soc. 2002, 149, A115.
Electrolyte Solutions for Rechargeable Magnesium Batteries Based on Organomagnesium Chloroaluminate Complexes
- [46] D. Aurbach, I. Weissman, Y. Gofer, E. Levi, Chem. Rec., 2003, 3, 61.
Nonaqueous Magnesium Electrochemistry and Its Application in Secondary Batteries (Review)
- [47] H. Yuan, X. Liu, J. Cao, L. Jiao, M. Zhao, Y. Wang, Battery Bimonthly, 2004, 34, 138.
The development of organic electrolyte for rechargeable magnesium battery (Review)
- [48] T. Ichitsubo, T. Adachi, S. Yagi, T. Doi, J. Mater. Chem., 2011, 21, 11764.
Potential positive electrodes for high-voltage magnesium-ion batteries
- [49] P. Novak, J. Desilvestro, J. Electrochem. Soc., 1993, 140, 140.
Electrochemical Insertion of Magnesium in Metal Oxides and Sulfides from Aprotic Electrolytes

- [50] K. Makino, Y. Katayama, T. Miura, T. Kishi, J. Power Sources, 2001, 99, 66.
Electrochemical insertion of magnesium to $\text{Mg}_{0.5}\text{Ti}_2(\text{PO}_4)_3$
- [51] X. Li, Y. Li, J. Phy. Chem. B, 2004, 108, 13893.
 MoS_2 Nanostructures - Synthesis and Electrochemical Mg^{2+} Intercalation
- [52] Z. Feng, J. Yang, Y. NuLi, J. Wang, J. Power Sources, 2008, 184, 604
Sol-gel synthesis of $\text{Mg}_{1.03}\text{Mn}_{0.97}\text{SiO}_4$ and its electrochemical intercalation behavior
- [53] Y. Liang, R. Feng, S. Yang, H. Ma, J. Liang, J. Chen, Adv. Mater., 2011, 23, 640.
Rechargeable Mg Batteries with Graphene-like MoS_2 Cathode and Ultrasmall Mg Nanoparticle Anode
- [54] P. Novak, W. Scheifele, O. Haas, J. Power Sources, 1995, 54, 479
Magnesium insertion batteries - an alternative to lithium
- [55] M. E. Spahr, P. Novak, O. Haas, R. Nesper, J. Power Sources, 1995, 54, 346
Electrochemical insertion of lithium, sodium, and magnesium in molybdenum(VI) oxide
- [56] 吉野崇史, 谷口耕治, 谷雲鵬, 桂ゆかり, 高木英典, 電気化学会第 80 回大会, 2013, 3H08.
クラスター化合物 $\text{M Mo}_9\text{Se}_{11}$ ($\text{M}=\text{Li}, \text{Mg}$) の二次電池正極特性
- [57] C. F. Fischer, ATOMIC DATA, 1972, 4, 301.
Average-energy-of-configuration Hartree-Fock results for the atoms Helium to Radon
- [58] W. A. Harrison. Electronic Structure and the Properties of Solids.
- [59] M. K. Aydinol, A. F. Kohan, G. Ceder, K. Cho, J. Joannopoulos, Phys. Rev. B, 1997, 56, 1354.
Ab initio study of lithium intercalation in metal oxides and metal dichalcogenides.
- [60] M. S. Whittingham, United States Patent, 1978, US 4084046.
Rechargeable electrochemical cell with cathode of stoichiometric titanium disulfide.
- [61] E. Levi, E. Lancry, A. Mitelman, D. Aurbach, G. Ceder, D. Morgan, O. Isnard, Chem. Mater. 2006, 18, 5492.
Phase Diagram of Mg Insertion into Chevrel Phases, $\text{Mg}_x\text{Mo}_6\text{T}_8$ ($\text{T} = \text{S}, \text{Se}$). 1. Crystal Structure of the Sulfides
- [62] D. Aurbach, G. S. Suresh, E. Levi, A. Mitelman, O. Mizrahi, O. Chusid, M. Brunelli, Adv. Mater., 2007, 19, 4260.
Progress in Rechargeable Magnesium Battery Technology
- [63] M. S. Whittingham, Prog. Solid St. Chem., 1978, 12, 41.
Chemistry of intercalation compounds: metal guests in chalcogenide hosts

- [64] R. R. Haering, J. A. R. Stiles, K. Brandt, United States Patent, 1980, US 4224390.
Lithium molybdenum disulphide battery cathode
- [65] R. Zhang, X. Yu, K.-W. Nam, C. Ling, T. S. Arthur, W. Song, A. M. Knapp, S. N. Ehrlich, X.-Q. Yang, M. Matsui, *Electrochemistry Communications*, 2012, 23, 110.
 α -MnO₂ as a cathode material for rechargeable Mg batteries
- [66] 吉野崇史. 修士論文, 2014.
マグネシウム二次電池正極材料の開拓

7 List of Publications

- (1) Yunpeng Gu, Kouji Taniguchi, Ryosuke Tajima, Shin-ichi Nishimura, Atsuo Yamada, Hidenori Takagi, J. Mater. Chem. A, 2013, 1, 6550.
A new "zero-strain" material for electrochemical lithium insertion

8 List of Patents

- (1) 吉野崇史, 谷口耕治, 谷雲鵬, 高木英典, 日本特許, 2012, JP 15B125002-1
マグネシウムイオン二次電池用正極活物質

9 List of Presentations

(International)

- (1) 62nd Annual Meeting of the International Society of Electrochemistry, Symposium 8a, Niigata, Japan, 2011
Cathode Performance of a New Spinel Oxide LiRh_2O_4
- (2) Project Meeting of the Strategic UK-Japan Cooperative Programme, Session 5, Scottish Borders, UK, 2011
Cathode Performance of a New Spinel Oxide LiRh_2O_4
- (3) Project Meeting of the Strategic UK-Japan Cooperative Programme, Tokyo, Japan, 2012.
Electrochemical Insertion of Lithium into a New Spinel Oxide LiRh_2O_4
- (4) GCOE International Symposium on Physical Sciences Frontier, No. 1-10, Tokyo, Japan, 2012.
Electrochemical Insertion of Lithium into a New Spinel Oxide LiRh_2O_4

(Domestic)

- (5) 電気化学会第 78 回大会, 1L23, 2011 年.
新規スピネル酸化物 LiRh_2O_4 の正極特性
など計 3 件

Acknowledgement

I would like to express my best gratitude to my supervisor Prof. H. Takagi for the excellent guidance during my Ph.D., who has offered me the opportunity to study at the University of Tokyo. I would like to send my deepest appreciation to Lecturer K. Taniguchi for his kind advices on this work all along.

This work could not have been done without useful suggestions from both present and former faculty and research staff including Prof. Itaka, Dr. Y. Nakamura, Dr. T. Takayama, Dr. Y. Katsura and Dr. D. Hirai, as well as cooperative contributions from scientists in other departments or research institutes including Prof. A. Yamada, Dr. S. Nishimura, Dr. D. Hashizume, Dr. Y. Okamoto and Mr. H. Oki.

I would also like to thank students for discussions on this work, including Mr. Y. Lu, Mr. H. Kawasoko, Mr. Y. Tashiro, Mr. Y. Tajima, Mr. H. Ishikawa Mr. T. Yoshino, Mr. A. Kato, Mr. M. Nakamura, Mr. R. Kawakami and Mr. A. Nakamura. My special thanks go to secretaries including Ms. K. Yashima, Ms. M. Imahori, Ms. K. Ichikawa and Ms. R. Matsunaga.

I am grateful to Prof. K. Terashima and Prof. N. Kida for the insightful comments in my Ph. D. defense.

This work has received experimental support from Ube Industries Ltd., and has been financially supported by JSPS through its "Funding program for World-Leading Innovative R&D on Science and Technology (FIRST Program)".

Finally, I would like to express my acknowledgement to all the people who helped me throughout the entire Ph.D. course.

August 2013
Yunpeng Gu